Pure Appl. Geophys.

DOI 10.1007/s00024-016-1314-z

Pure and Applied Geophysics

Regional Ambient Noise Tomography in the Eastern Alps of Europe

Michael Behm,[1,2] Nori Nakata,[2,3] and Götz Bokelmann[1]

Abstract—We present results from ambient noise tomography applied to temporary seismological stations in the easternmost part of the Alps and their transition to the adjacent tectonic provinces (Vienna Basin, Bohemian Massif, Southern Alps, Dinarides). By turning each station into a virtual source, we recover surface waves in the frequency range between 0.1 and 0.6 Hz, which are sensitive to depths of approximately 2–15 km. The utilization of horizontal components allows for the analysis of both Rayleigh and Love waves with comparable signal-to-noise ratio. Measured group wave dispersion curves between stations are mapped to local cells by means of a simultaneous inverse reconstruction technique. The spatial reconstruction for Love-wave velocities fails in the central part of the investigated area, and we speculate that a heterogeneous noise source distribution is the cause for the failure. Otherwise, the obtained group velocity maps correlate well with surface geology. Inversion of Rayleigh-wave velocities for shear-wave velocities along a vertical N-S section stretching from the Bohemian Massif through the Central Alps to the Southern Alps and Dinarides reveals a mid-crustal low-velocity anomaly at the contact between the Bohemian Massif and the Alps, which shows a spatial correlation with the P-wave velocity structure and the low-frequency component of the magnetic anomaly map. Our study is validated by the analysis of resolution and accuracy, and we further compare the result to shear-wave velocity models estimated from other active and passive experiments in the area.

1. Introduction

Ambient noise tomography (ANT) has become a standard tool among seismologists for subsurface characterization. The method relies on extraction of signal, predominantly surface waves, from continuous seismic recordings, without the need of any active or well-defined sources. Although the initial idea dates back to Aki (1957), the technique has become particularly popular over the last 10 years due to the availability of massive amounts of digital seismological data from all over the world, further theoretical developments (e.g., Lobkis and Weaver 2001; Snieder 2004; Wapenaar 2004; Roux *et al.* 2005), and the availability of data processing tools. A good overview and practical introduction to ANT has been given by Bensen *et al.* (2007). ANT proves to be very successful in recovering surface waves that constrain the structure of crust and uppermost mantle. Over the last decade, there have been applications to many if not most parts of the world, beginning with Mexico (Campillo and Paul 2003) and California (Shapiro *et al.* 2005). Surface waves readily emerge from long-term waveform correlation of ambient noise. This is much less the case for body waves, since their already weak amplitudes are further downweighted by the stacking procedure employed, and because of a much less-suited source distribution (e.g. Forghani and Snieder 2010). Nonetheless, body-wave reconstruction from regional and teleseismic earthquakes as well as from ambient noise has been demonstrated by several studies (e.g. Draganov *et al.* 2009; Landes *et al.* 2010; Schimmel *et al.* 2011a; Nakata *et al.* 2014, 2015; Olivier *et al.* 2015).

Historically, applications of ANT grew out of the global seismology community, fuelled by the availability of continuously recording broadband instruments all over the world. The main results are frequency-dependent Rayleigh-wave velocity maps covering large tectonic provinces or entire continents, e.g., California (Shapiro *et al.* 2005), the Pacific Northwest (Moschetti *et al.* 2007; Yang *et al.* 2008), Tibet (Yao *et al.* 2006), South Korea (Cho *et al.* 2006), Europe (Villasenor *et al.* 2007; Yang *et al.* 2007; Verberke *et al.* 2012), and New Zealand (Lin *et al.* 2007). Stehly *et al.* (2009) have applied

[1] Department of Meteorology and Geophysics, University of Vienna, Vienna, Austria. E-mail: Michael.Behm@univie.ac.at
[2] ConocoPhillips School of Geology and Geophysics, University of Oklahoma, Norman, USA.
[3] Department of Geophysics, Stanford University, Stanford, USA.

Published online: 25 May 2016

ambient noise interferometry for Central Europe and subsequently deduced Moho depths for the Alps from their results. In the Western Alps, Fry *et al*. (2010) combined ANT with the simultaneous estimation of crustal anisotropy. Macquet *et al*. (2014) introduced a non-linear inversion scheme to invert for a 3D shear-wave velocity model of the heterogeneous crust below the Pyrenees. Beside these regional-scale applications, several studies have demonstrated also the applicability of ANT for local targets (Bussat and Kugler 2009; Picozzi *et al*. 2009; de Ridder and Dellinger 2011; Nakata *et al*. 2011, Behm *et al*. 2014).

In this paper, we present results from a regional deployment in the Eastern Alps of Austria. During the ALPASS project, 32 short-period and 25 broadband stations recorded continuously from May 2005 to May 2006 in a 350 by 250-km wide area (Fig. 1). Data from the ALPASS project were subject to teleseismic tomography (Mitterbauer *et al*. 2011) and receiver function studies (Bianchi and Bokelmann 2014; Bianchi *et al*. 2014, 2015). Our study aims at extracting surface waves from the continuous recordings; for that purpose, we combine the ALPASS data set with stations from the CBP deployment (Dando *et al*. 2011) in the easternmost part of Austria. Several other passive experiments have been conducted in adjacent areas recently and provide information on the crustal structure based on ANT. Li *et al*. (2010a) and (2010b) calculate both Rayleigh and Love-wave velocity maps from 114 stations for the Italian peninsula, and they subsequently derive a 3D shear-wave velocity model of the crust and uppermost mantle. Fry *et al*. (2010) analyse ambient noise recorded at the Swiss national network, especially in light of azimuthal variations of Rayleigh-wave phase velocities. Ruzek *et al*. (2012) combine receiver function analysis and ANT for the region of the Bohemian Massif and also derive group velocity maps for both Rayleigh and Love waves. Ren *et al*. (2013) investigate the CBP data set for the wider Pannonian and Carpathian region and derive a comparably well-resolved 3D shear-wave velocity model of the upper 50 km of the lithosphere based on Rayleigh waves. Our interpretation of the ALPASS data set closes a small, but tectonically a significant gap in the easternmost part of the Alps in-between these four studies.

Since the Eastern Alpine area has been studied much less than the other parts of Europe, there are important open questions that may in principle be shed light on by an ambient noise study. There is an interesting variety of tectonic features in this area, where the Alps meet the Bohemian Massif, the Carpathians, and the Dinarides, raising questions as to how the deep structure is associated with surface geology and tectonics. In the area of the Vienna basin, the crustal structure is only weakly constrained, even though it has a significant societal importance due to potentially under-estimated seismic hazard (e.g. Hinsch and Decker 2003) and its relation to the hydrocarbons in the sediments (Brix 1993). In addition, the structure below the depths that ANT can resolve is of great interest, and there are several models (e.g., Lippitsch *et al*. 2003; Mitterbauer *et al*. 2011; Qorbani *et al*. 2015), but no consensus yet. It is important to better understand the crustal structure, since it may affect and complement images of the deeper structure. Our study should also be seen in the light of the upcoming AlpArray initiative which aims at large-scale passive seismic recording in the entire Alpine orogen (Kissling *et al*. 2014), because the analysis and review of all existing data sets should be mandatory prior to new acquisition.

2. *Tectonic and Geologic Setting*

The Eastern Alps have formed as a consequence of the continent–continent collision between the European and Adriatic-Apulian plates in the Eocene, and have later been modified by eastward-directed extension/escape tectonics starting in the late Oligocene (Gutdeutsch and Aric 1988; Ratschbacher *et al*. 1991), resulting in a complex three-dimensional seismic structure of the lithosphere. Schmid *et al*. (2004) give a summary on the structure and evolution of the entire alpine orogen from a plate-tectonic perspective. Based on recent seismic data and a wealth of complementary information, Brückl *et al*. (2010) present a geodynamic model for the

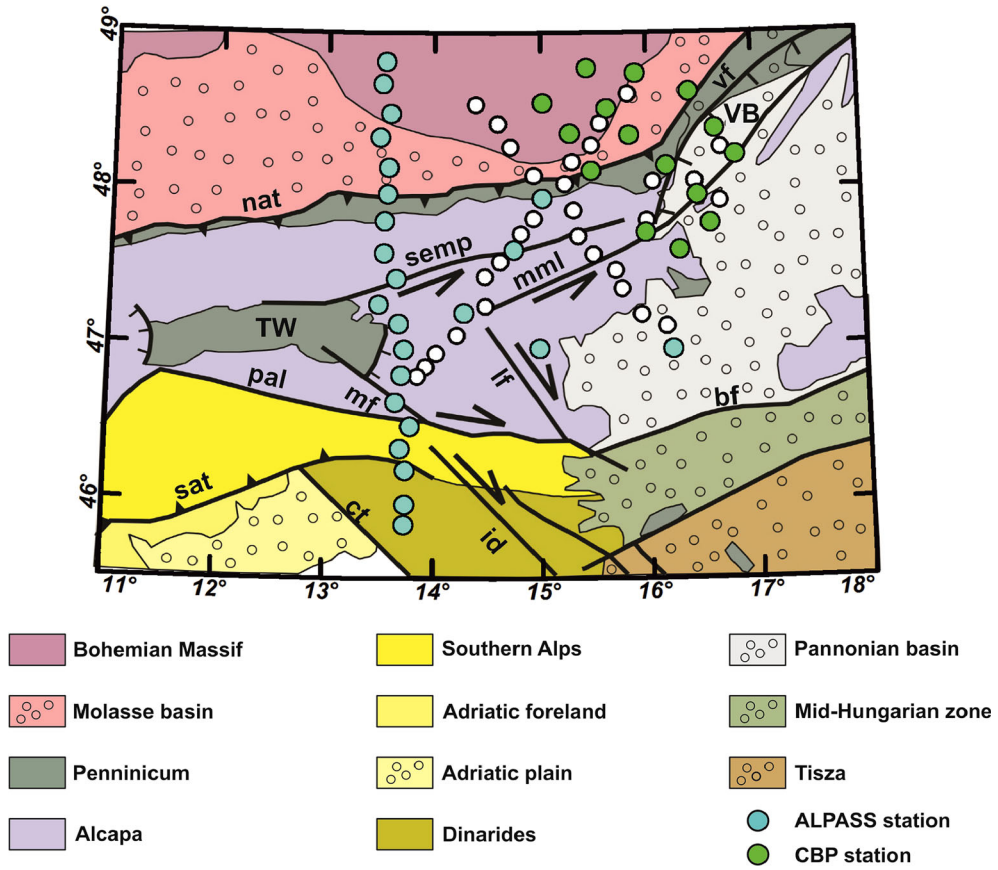

Figure 1
Geologic/tectonic map of the investigated area (based on Brückl *et al.* 2010) and location of broadband stations (*cyan* and *green circles*). *Small white circles* indicate ALPASS short-period stations which are not used in this study. *TW* Tauern window; *VB* Vienna basin; *nat* North Alpine thrust; *semp* Salzach-Enns-Mariazell-Puchberg line; *vf* Vienna basin transfer fault; *mml* Mur-Mürz line; *pal* Periadriatic line; *mf* Malta fault; *lf* Lavant Valley fault; *sat* South Alpine thrust; *ct* Cicarija fault; *id* Idria fault; *bf* Balaton fault

easternmost part of the Alps and postulate a stable continental triple junction in the area of the south-eastern margin of the Tauern Window. According to their interpretation, the lithospheric fragment Pannonia (Behm *et al.* 2007; Brückl *et al.* 2007) got detached from the Adriatic realm during the extension phase, and its movement to the East was further facilitated by the Carpathian rollback (Royden 1993; Peresson and Decker 1997).

The investigated area of this study (Fig. 1) encompasses young and deep sedimentary basins (Vienna basin, Molasse basin; Fig. 2), old (paleozoic) igneous platforms (Bohemian Massif), prominent thrust and strike-slip systems (Northern Alpine Thrust, Salzach–Enns–Mariazell–Puchberg line, Periadriatic line, Mur-Mürz line), uplifted metamorphic core complexes (Tauern Window), and thick thrust sheets comprising a melange of sedimentary, metamorphic, and igneous rocks (Penninicum, Alcapa, Southern Alps, Dinarides). This complex tectonic setting manifests itself in both a multifaceted map of the surface geology and intricate images of the crust where available (Graßl *et al.* 2004; Lüschen *et al.* 2006; Brückl *et al.* 2007; Behm *et al.* 2007; Behm 2009; Grad *et al.* 2009; Bianchi and Bokelmann 2014; Qorbani *et al.* 2015).

3. Data Processing

The ALPASS network operated from May 2005 to June 2006. We use data from the 25 broadband

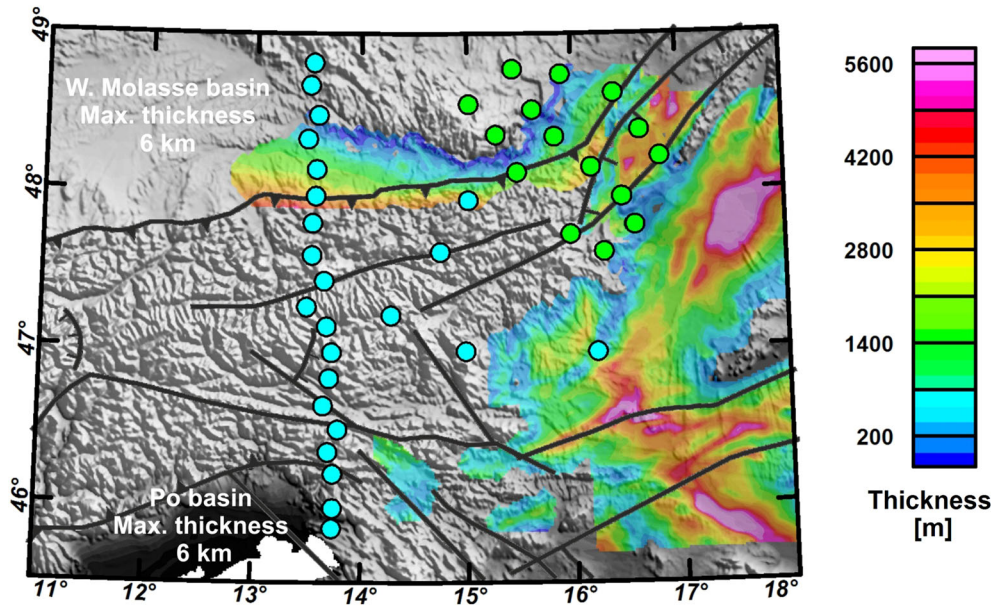

Figure 2
Digital terrain model and thickness of tertiary sediments in the investigated area. Superimposed are the locations of used broadband stations (*cyan* and *green circles*). For the Western Molasse and Po Basins, only the maximum thicknesses are indicated

stations only, since the lower limit of the targeted frequency range is 0.05 Hz, and is thus below the natural frequency of the short-period stations (1 Hz and higher). In addition to the ALPASS network, we also include 15 broadband stations from the CBP network (Dando *et al*. 2011). Specifications and deployment duration of the individual instruments are listed in Appendix. We create virtual source gathers (Bakulin and Calvert 2006) by correlating the recording of one receiver (the virtual source) with all others (Figs. 3, 4). Each correlated trace is referred to as an interferogram (Wapenaar *et al*. 2010a; Schuster 2010). Data pre-processing and calculation of the interferograms follow the routines outlined in Bensen *et al*. (2007) and Behm *et al*. (2014), and we create interferograms for the vertical, radial, and transverse components. The radial direction is defined as the azimuth from the virtual source to the receiver, and the transverse direction is radial +90°. We refer to Behm *et al*. (2014) and Lin *et al*. (2008) for a discussion on interferometry of horizontal component data and requirements for pre-processing.

Pre-processing commences with downsampling of all recordings to 4 Hz. We estimate the lower threshold of the usable frequencies from $f_{\min} = c_{\min}/\lambda_{\max}$, where $c_{\min}$ is the lowest expected velocity and $\lambda_{\max}$ the largest expected wavelength. $\lambda_{\max}$ is calculated as a third of the maximum station spacing (360 km) to avoid overlap of causal and acausal arrivals (Bensen *et al*. 2007). Assuming a minimum surface-wave velocity of 2000 m/s, $f_{\min}$ calculates to 0.017 Hz. This is the theoretical value for the lowest frequency which we expect to recover by interferometry. However, the average station spacing is smaller (120 km), and thus the lowest observable frequency for most station pairs will be larger. Initial tests show that, even for the smallest station spacing, spatially coherent noise is restricted to maximum frequencies of about 0.5 Hz. We apply a zero-phase bandpass filter ranging from 0.005 to 0.9 Hz to the data, and amplitudes are temporally normalized by automatic gain control (AGC) with a window length of 0.1 s. With regard to the sampling interval (0.25 s), the short AGC time window effectively operates as one-bit normalization, but it has the advantage of being commutative with rotation of the horizontal components. In case of a receiver array which is not strictly deployed along a line or a great circle, the azimuthal variation of the virtual source—receiver pairs would require the rotation to be applied

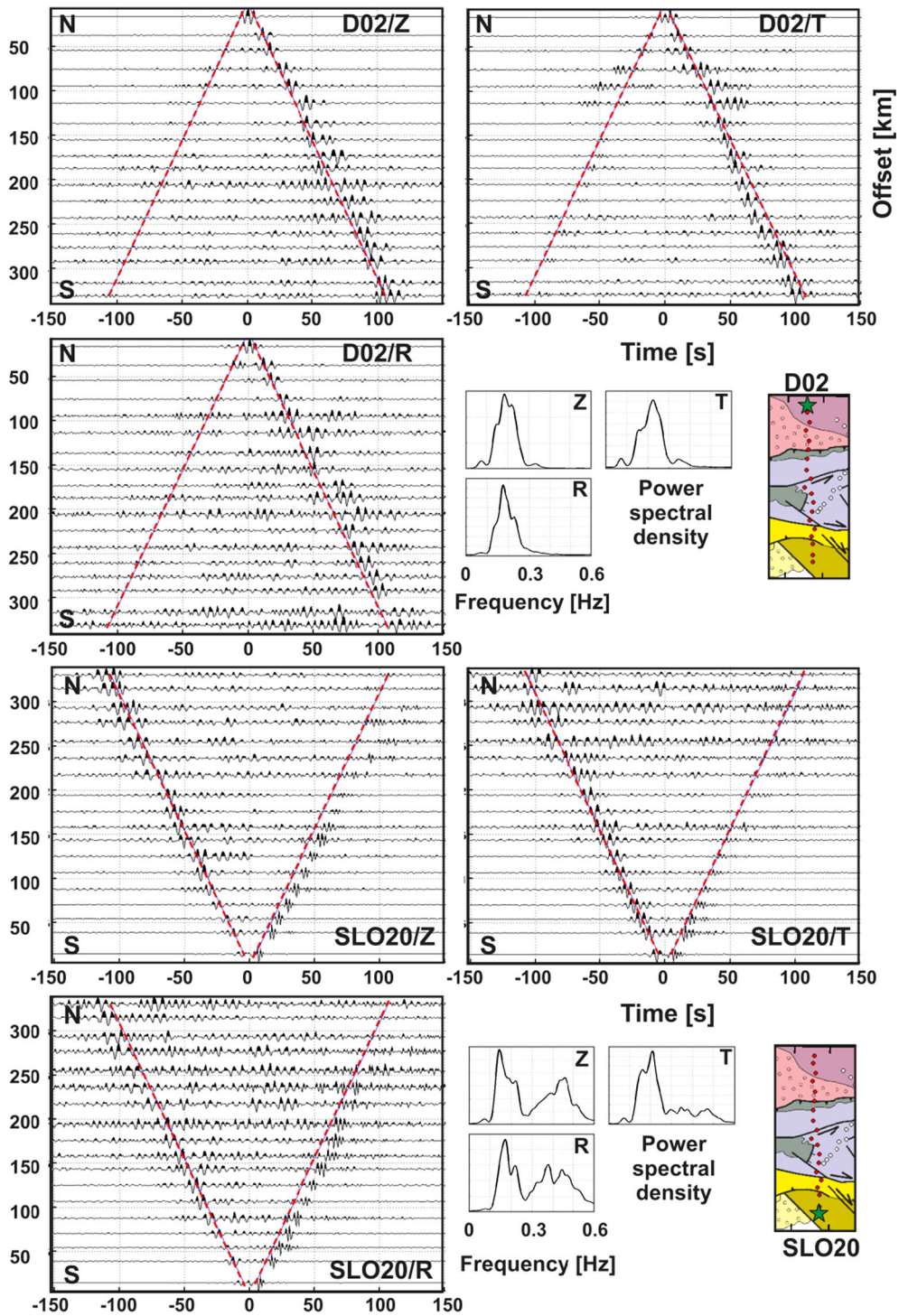

Figure 3
Virtual source gathers for stations of profile ALPASS 1 with D02 (*4 panels* on the *top*) and SLO20 (*4 panels* on the *bottom*). All three components (vertical *Z*, radial *R*, transverse *T*) are shown. The *red dashed line* indicates a linear move-out for a velocity of 3.1 km/s. The traces are spaced according to their offset to the virtual source station. See text for details

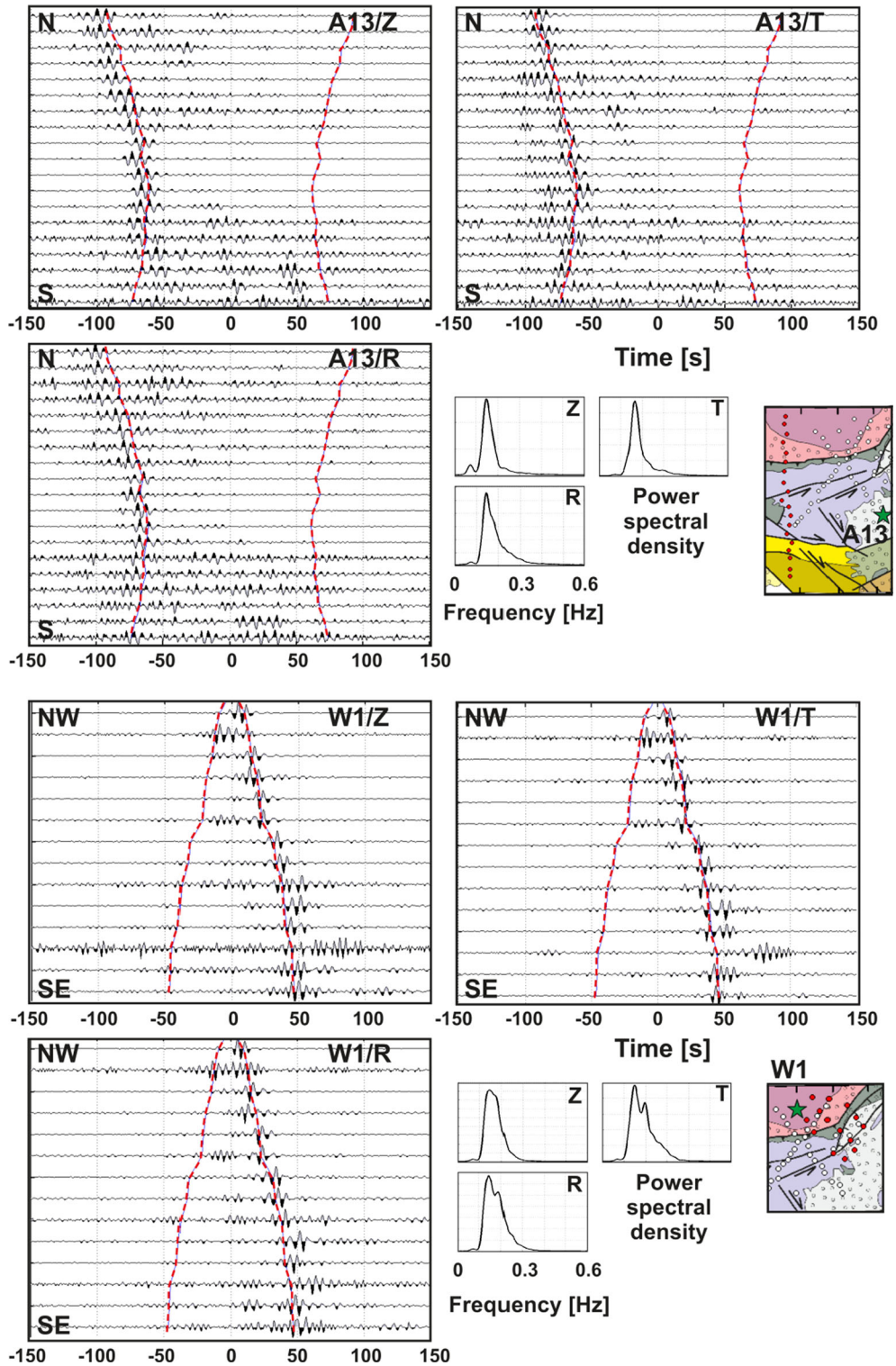
N
A13/Z
S
-150 -100 -50 0 50 100
N
A13/T
S
-150 -100 -50 0 50 100 150
Time [s]
N
A13/R
S
-150 -100 -50 0 50 100 150
Z
T
R
Power spectral density
0 0.3 0.6
Frequency [Hz]
A13
NW
W1/Z
SE
-150 -100 -50 0 50 100
NW
W1/T
SE
-150 -100 -50 0 50 100 150
Time [s]
NW
W1/R
SE
-150 -100 -50 0 50 100 150
Z
T
R
Power spectral density
0 0.3 0.6
Frequency [Hz]
W1

◀Figure 4
Virtual source gathers for stations of profile ALPASS 1 with station A13 (*top panels*) and for station W1 (*bottom panels*). All three components (vertical *Z*, radial *R*, transverse *T*) are shown. The *red dashed line* indicates a linear move-out for a velocity of 3.1 km/s, which appears curved, since neither station A13 nor W1 are located on the ALPASS 1 profile. See text for details

before the normalization. The implemented form of the AGC for the horizontal component data (Lin *et al.* 2008; Behm *et al.* 2014) allows reversing this sequence, which requires less computational effort.

Pre-processing concludes with spectral whitening, which aims at equalizing energy across frequency bins and suppressing monochromatic signals in the chosen frequency band. It is noted that spectral whitening is an intrinsic part of the interferogram calculation by the method of cross-coherence as applied in this study, and this pre-processing step may be deemed as redundant. However, future interferometric analysis of the data might employ different correlation schemes, and therefore, the preparation of a homogenous input data set is preferred. The same line of thought as for normalization applies for whitening of horizontal component data, and the actual implementation of this pre-processing step ensures commutativity with rotation (Lin *et al.* 2008; Behm *et al.* 2014). Finally, we rotate the horizontal components into the radial (*R*) and transverse (*T*) directions. For all three components (Z, R, T), we cut the pre-processed data of the entire observation period into one-day-long time windows $x^{(i)}(t)$ and apply the Fourier transform to obtain the spectral representation $X^{(i)}(f)$, where the superscript (i) denotes a specific time window. For a given station pair (*A* virtual source; *B* receiver) and each time window, we calculate an individual interferogram $Y^{(i)}_{AB}(f)$ in the spectral domain by cross-coherence (Aki 1957; Wapenaar *et al.* 2010b; Prieto *et al.* 2009):

$$Y^{(i)}_{AB}(f) = \frac{X^{(i)}_B(f) \cdot \overline{X^{(i)}_A(f)}}{\left\|X^{(i)}_B(f)\right\| \cdot \left\|X^{(i)}_A(f)\right\| + \varepsilon^2} \qquad (1)$$

In Eq. (1), the overbar denotes the complex conjugate. ε is introduced to avoid instabilities that may occur if either $X^{(i)}_A(f)$ or $X^{(i)}_B(f)$ approaches zero. ε is taken as 0.5 % of the average amplitude spectrum of $X^{(i)}_A(f)$ and $X^{(i)}_B(f)$. The final interferogram $G_{AB}(f)$ is obtained by stacking over all N individual interferograms:

$$G_{AB}(f) = \sum_{i=1}^{N} Y^{(i)}_{AB}(f) \qquad (2)$$

The inverse Fourier transformation is applied and the resulting time representation $g_{AB}(t)$ is an approximation to the Green's function between the stations *A* and *B*. Instead of cutting the data into time windows and stacking the individual interferograms, one can also correlate the recordings of the entire observation period to get $G_{AB}(f)$. We find time windowing and stacking more efficient with respect to testing processing parameters, and the actual implementation of our interferometry algorithm allows for parallelization when the data are organized in time windows (Behm *et al.* 2014). In this study, we calculate interferograms for the vertical (Z–Z), radial (R–R), and transverse (T–T) components, but not the cross-component interferograms (Z–R, Z–T, R–T). The cross-component interferograms would allow evaluating an estimate of the full Green's tensor, which, however, is outside the scope of this study. For many reasons (e.g., source signature, instrument noise, attenuation, scattering phenomena, and measurement of displacement instead of stress; Snieder 2007; Halliday and Curtis 2008; Tsai 2011), the obtained interferogram $g_{AB}(t)$ is only an approximation to the actual Green's function and therefore, an estimate of the impulse response of the earth. Thus, Green's functions recovered by interferometry might be considered as empirical Green's functions.

Figures 3 and 4 show several virtual source gathers along the profile ALPASS 1 and for the CBP array. The virtual source station D02 (Fig. 3) is located in the Bohemian Massif at the northern end of the profile. On all three components, there are clear arrivals in the causal parts of the interferograms, but much less so on the non-causal part. Such an asymmetry is generally thought to result from an uneven distribution of seismic sources (e.g. Harmon *et al.* 2010). This does not necessarily imply that the results are biased towards wrong velocities, as long as the stationary phase condition (Snieder 2004) is met for sources at either side of the virtual source—receiver

pair. In the shown example, the ambient noise sources are apparently much stronger to the North of the deployment than to the South. As in other regional and global ambient noise studies (e.g. YANG and RITZWOLLER 2008; SCHIMMEL *et al*. 2011b), the dominant seismic source is assumed to be the interaction of ocean waves with the shore and/or the continental shelf (LONGUET-HIGGINS 1950). In the context of ocean-generated ambient noise, STEHLY *et al*. (2006) were the first to discuss how the distribution of noise sources influence the symmetry of the correlations. Among others, FRIEDRICH *et al*. (1998), CHEVROT *et al*. (2007), and KEDAR *et al*. (2008) discussed the origin of seismic noise in Europe. In our study, the North Sea would indeed represent a major source region of ambient seismic noise energy.

The dominant frequency content ranges between 0.1 and 0.3 Hz, and the apparent velocity is about 3.1 km/s on the Z- and R-components. The arrivals on the T-component appear significantly earlier. Even at large offsets (>300 km), the waveforms are of high S/N ratio. The Z- and T-component interferograms are of higher S/N ratio than the R-component. Station SLO20 (Fig. 2) is located in the Dinarides at the southern end of the profile, and the waveforms in the acausal parts are of similar characteristics (frequency content, S/N ratio, apparent velocity) as for station D02. This suggests similar if not identical ambient noise sources to the north of the deployment. Additional arrivals with higher frequencies (0.3–0.5 Hz) are observed up to 200 km offset at the Z- and R-components in the causal part, and to a lesser significance, also at the T-component. The ambient noise sources for these arrivals must be located rather to the South of the profile. Compared to the Eastern Alps and the Bohemian Massif, the Dinarides are seismically more active and local and regional seismicity could explain the causal arrivals with lower energy and higher frequency.

Virtual source station A13 (Fig. 4) is located to the east of profile ALPASS 1. The arrivals appear in the acausal part only, suggesting dominant ambient noise sources to the west (Atlantic Ocean) and northwest (North Sea) of the deployment. The damping of the higher frequencies (>0.2 Hz) is explained by the large virtual source—receiver distances, which in this cross-line example affects all receiver stations. Again, the T-component arrivals are faster than the arrivals on the Z- and R-components. Finally, virtual source station W1 (Fig. 4) represents an example from the CBP data. Overall, the waveforms at the CBP stations appear less clear, which may be attributed to a different instrument response (Appendix) and a more complicated near-surface structure with its abrupt transition from high-velocity carbonates (Eastern Alps) and crystalline rocks (Bohemian Massif) to thick low-velocity sediments (Flysch, Vienna Basin). Apart from that, the acausal/causal characteristics as well as the frequency content and the apparent velocities are similar to the other examples.

As in other studies (LIN *et al*. 2008; LI *et al*. 2010a, b; BEHM *et al*. 2014; BEHM and SNIEDER 2013), we interpret the arrivals on the vertical and radial components as Rayleigh waves and the arrivals at the transverse component as Love waves. The Love waves are faster than the Rayleigh waves, as is expected for isotropic media. In the investigated area, strong anisotropy (10 %) is only known locally in the shallow part (<3 km-depth) of the Tauern Window in the Central Alps due to north-dipping foliation (Bleibinhaus and Gebrande 2006). On a regional scale, 3D P- and S-wave modelling from active-source data do not indicate a significant anisotropy (BEHM *et al*. 2007; BEHM 2009). The velocity difference is also illustrated in Fig. 5, where we stack envelopes (modulus of the complex trace) of all interferograms in offset bins. The envelope is applied, since local and regional velocity variations cause the individual surface wave arrivals to be out of phase with respect to their large offset variations. The offset-bin stacks show that the arrivals on the Z- and R-components have identical average velocities (slightly lower than 3.1 km/s), and that the T-component arrivals have a velocity above 3.1 km/s. This difference of velocities indicates that the rotation of the components works well to separate wavefield polarities. Furthermore, the S/N ratio of the interferograms is comparable for the Z- and T-components, and lowest on the R-component. This implies that the horizontal component of the Rayleigh wave has lower amplitude than its vertical component. This latter effect is also observed on both global (LIN *et al*. 2008) and local (BEHM *et al*. 2013) scales, and is

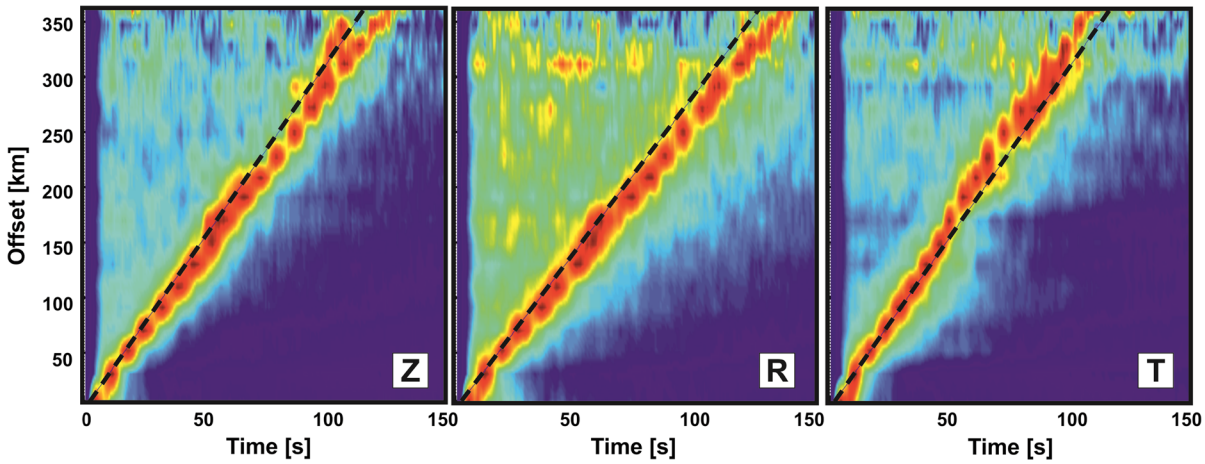

Figure 5
Offset-bin stacks of all interferograms for the three components (vertical *Z*, radial *R*, transverse *T*). The offset-bin size is 20 km. The *dashed line* indicates a linear move-out for a velocity of 3.1 km/s. Note the overall lower velocities of the vertical and transverse components compared to the transverse component

consistent with what is expected from the "upright" elliptical particle motion of fundamental-mode Rayleigh waves at the Earth's surface (AKI and RICHARDS 1980).

4. Dispersion Measurements and Inversion

4.1. Frequency-Time Analysis

Frequency-time analysis (FTAN; DZIEWONSKI *et al.* 1969; LEVSHIN *et al.* 1989; BENSEN *et al.* 2007) is commonly applied to surface-wave interferograms to obtain group velocity dispersion between two stations. In essence, FTAN applies narrow Gaussian-shaped bandpass filters for a range of central frequencies to the interferogram. A complex trace is derived from the original trace (real part) and its Hilbert transform (imaginary part). The modulus of the complex trace is the envelope, and the time axis of the trace is converted to velocity by dividing through its offset. Thus, the maximum amplitude of the envelope corresponds to the group velocity of the surface wave for the given central frequency. The original FTAN algorithm operates with a halfwidth of the Gaussian function which increases with central frequency, which may cause data with low central frequencies to be under-sampled. Therefore, we chose a parameterization where the halfwidth is independent from the central frequency. A small halfwidth results in a monochromatic and thus ringing signal, which after the envelope transformation will have low resolution in the velocity domain, while a large halfwidth entails a low-frequency resolution. After testing, we chose a halfwidth of 0.095 Hz. Finally, the FTAN-plots are semi-automatically picked for dispersion curves at the maximum amplitude at each central frequency (Fig. 6).

As expected for Rayleigh and Love waves, the first three examples (Fig. 6a–c) show a similarity of the Z- and R-components, and comparably higher velocities at the T-component. In contrast, the dispersion curves from the Vienna Basin (Fig. 6d) exhibit a discrepancy between the Z- and R-components and slower T-component velocities, which is discussed in Sect. 5. The data allow measuring dispersion curves for 434 and 529 station pairs on the Z- and T-components, respectively. Since the S/N ratio of the R-component interferograms is lower than their equivalent Z-component counterparts, we only pick dispersion curves from the Z- and T-components and use them for estimating Rayleigh and Love velocities. The assumption that the Rayleigh waves appear on Z- and R-components and Love waves on the T-component is valid for a horizontally layered medium (1D) only. While this first-order approximation may be applicable for deeper layers, the near

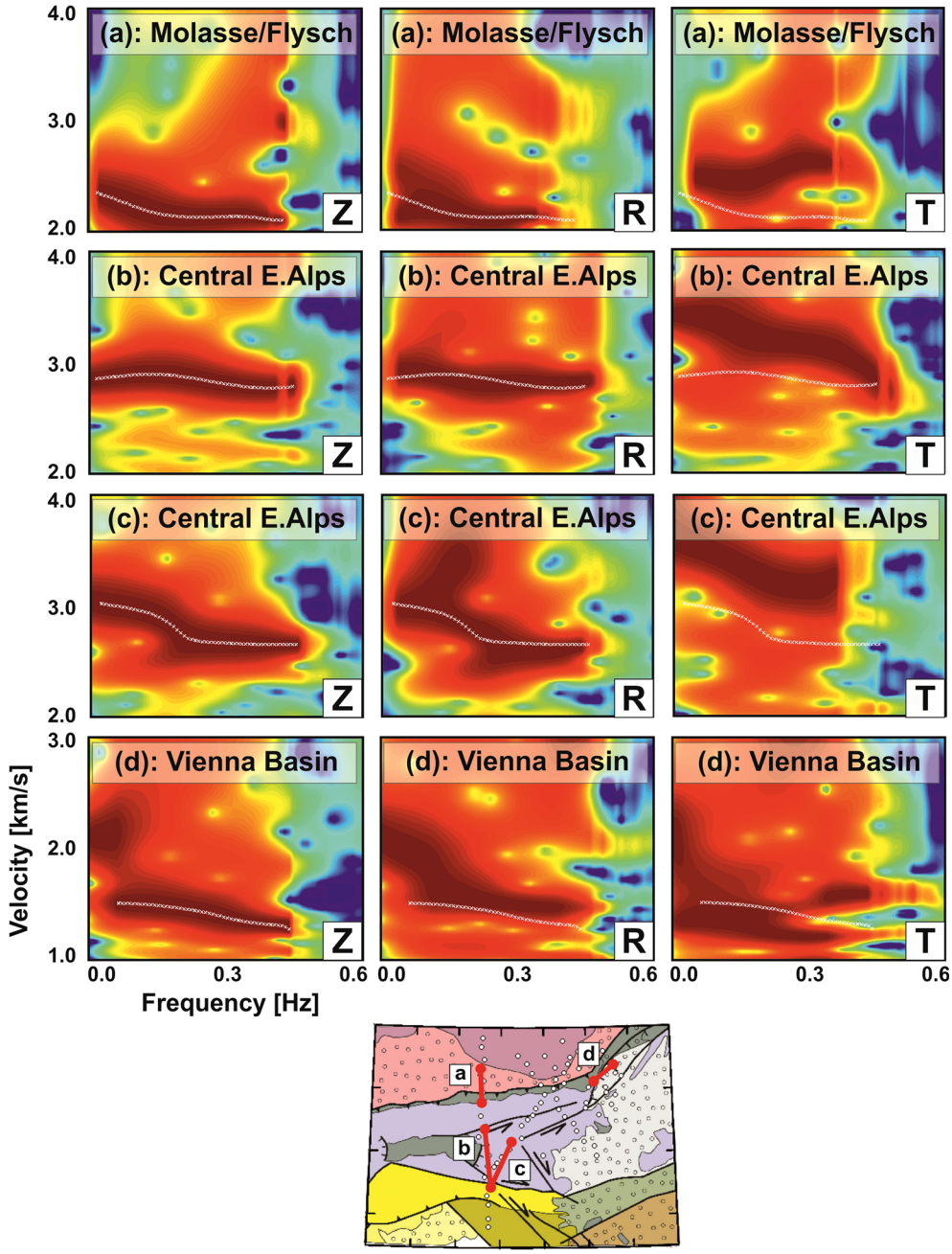

Figure 6

Group velocity dispersion measurements for four selected virtual source–receiver combinations and all three components. Ray paths of the virtual source–receiver combinations are shown in the map below. The *white line* indicates the picked dispersion curve for the vertical component, which is also superimposed on the radial and transverse components for comparison. Note the change in the velocity axis for figure (**d**). See text for details

surface in the Eastern Alps has an intricate 3D structure. Thus, the high-frequency part of the dispersion curves is interpreted with caution. As mentioned above, the full nine-component Green's tensor (Z–Z, R–R, T–T, Z–R, R–Z, Z–T, T–Z, R–T, and T–R correlations) could be used to investigate the

significance of 3D effects, but this is subject to further studies.

4.2. *Inversion for Frequency-Velocity Maps and Virtual Dispersion Curves*

Measured dispersion curves are easily interpreted if the velocity structure between the stations can be well approximated by a horizontally layered medium. The upper crust in the Eastern Alps deviates strongly from this 1D assumption though, and the surface waves sample different tectonic regimes along their path. This is especially the case when the offset between the stations is large. As a result, a consistent interpretation of the measured dispersion curves can become difficult. We tackle this challenge by taking advantage of the multifold coverage, and construct virtual dispersion curves which are representative of the 1D structure at specific locations. The specific location is defined as a cell of small, but still finite extent.

Assuming straight ray paths between station pairs (A–B), a location with a given lateral extent (a cell) is covered by many surface waves with measured group velocities $v_{AB}(f)$. The measured velocity depends on A and B and cannot be unambiguously assigned to a cell. Analogous to SIRT-based travel-time tomography (Simultaneous Inverse Reconstruction Technique; e.g., VAN DER SLUIS and VAN DER HORST 1987), we redistribute the measured velocities $v_{AB}(f)$ onto the cell velocities $v_{cell}(f)$ along the ray paths to better constrain their spatial assignment and facilitate geologic interpretation. The velocities are converted to slownesses (s_{AB}, s_{cell}) to establish a linear relationship between observations (s_{AB}) and unknowns (s_{cell}):

$$\frac{1}{v_{AB}(f)} = s_{AB}(f) = \frac{1}{x_{AB}} \cdot \sum_{i=1}^{N} s_{cell}^{(i)}(f) \cdot l^{(i)} \qquad (3)$$

Equation (3) assumes that the measured slowness $s_{AB}(f)$ is a weighted average of the localized slownesses $s_{cell}^{(i)}(f)$ in all N cells which the surface wave passes along its path from station A to station B. The weighting factor is the length $l^{(i)}$ of the surface wave ray in a cell. x_{AB} is the offset between the stations A and B, and therefore is the sum of all $l^{(i)}$. Given sufficient coverage [a large number of station pairs with measured slownesses $s_{AB}(f)$], an equation system based on (3) is built and inverted for the cell slownesses $s_{cell}^{(i)}(f)$ by damped least-squares inversion. We do not model cells with constant velocities, but chose a different parameterization by specifying velocities at the cell corners. The velocity along a ray segment $l^{(i)}$ is then interpolated from the surrounding cell corner points with the distance to each corner as a weighting factor. This results in a smoother velocity distribution, in particular when the cell size is large. The implementation is based on a scheme for calculating delay times (td_{SRC}, td_{RCV}) and refractor slownesses from observed travel times t_{AB} of refracted waves (GARDNER 1939; TELFORD *et al.* 1990; IWASAKI 2002; BEHM *et al.* 2007):

$$t_{AB} = td_{SRC} + \sum_{i=1}^{N} s_{cell}^{(i)}(f) \cdot l^{(i)} + td_{RCV} \qquad (4)$$

In Eq. (4), refractor travel times are simulated as $t_{AB} = x_{AB}/v_{AB}$, and the delay times (td_{SRC}, td_{RCV}) are fixed to zero; thus, Eq. (4) becomes Eq. (3).

We start from an initial homogenous cell slowness distribution of $(3000\ \mathrm{m/s})^{-1}$ and calculate the synthetic group slowness s_{AB} according to Eq. (3). The differences between the measured and synthetic group slownesses are inverted for cell slowness updates by damped least-squares inversion. The cell slowness updates are added to the initial slowness, and the obtained cell slowness solution is smoothed with a Gaussian-shaped low-pass filter. This process is iterated up to three times, with the damping and smoothing decreased at each iteration step. Although Eqs. (3) and (4) pose a linear relation between the unknown cell slownesses and the observed (measured) slownesses, iteration becomes necessary, since post-inversion smoothing introduces a small degree of non-linearity between unknowns and observations. The tomography with straight ray paths, as implemented here, is a simple version of more advanced methods which employ curved ray paths (e.g., RAWLINSON and SAMBRIDGE 2003). Like BEHM *et al.* (2014), we chose constant ray paths for robustness when input data are sparse and scattered. The presented implementation further allows for an additional qualitative check of the virtual dispersion curves.

We chose the cell size to be 20 km. Surface-wave velocities are defined between two locations, and therefore, the cell size is not directly related to geological structures. Much more, it represents a desired resolution based on the minimum inter-station distance in our network.

Figure 7 shows the ray paths of all measured dispersion curves from the vertical component, and the grid of cell corner points. The inversion is performed for slownesses grouped in frequency bins with sizes of 0.015 Hz. For each measured dispersion curve, we average the slowness in each frequency bin to obtain the input slowness $s_{AB}(f)$ to the equation system (3). The final results of the damped least-squares inversion are the localized slownesses (velocities) $s_{cell}(f)$ ($v_{cell}(f)$) of the cells specified at the grid points.

The Z-component data of the third iteration step result in overall strongly fluctuating velocity distributions, and the same applies for T-component data of the second iteration step. We subsequently chose the results from the second and first iteration steps as the preferred velocity models for Z- and T-component data, respectively (Figs. 8, 9). The damped least-squares inversion also provides resolution elements of the calculated cell velocities, and we discard cells with low resolution from the final solution. Table 1 gives a summary on the inversion results averaged over the entire frequency range of 0.05–0.5 Hz.

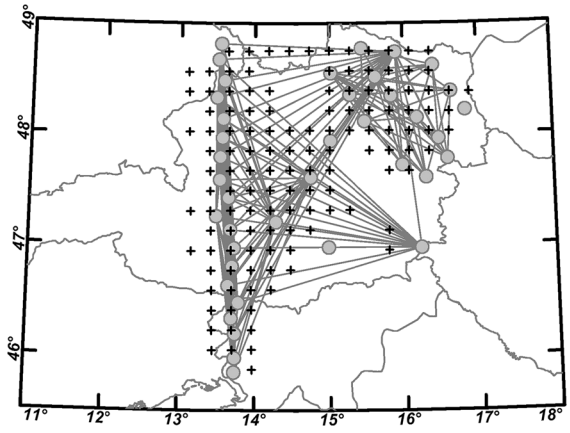

Figure 7
Observed ray paths for group velocity dispersion measurements on the vertical component. The *crosses* mark the center of the cells which are included in the tomographic inversion due to direct coverage or due to smoothness constraints at the edge

The inversion of Z-component data is deemed successful both in terms of misfit reduction and geologic plausibility. The latter is judged by the fact that the average velocity in each frequency bin is similar prior and after the inversion (Fig. 10). Since the inversion based on Eqs. (3) and (4) seeks for a lateral redistribution of the measured velocities, we expect similar average velocities within each frequency bin prior and after the inversion. In contrast, inverted velocities from T-component data are significantly different from the measured velocities. Their post-inversion average dispersion also has a bias towards high velocities in the mid-frequency range, and the misfit reduction is low (Table 1). We take this as an indication that the SIRT-based inversion of measured Love-wave velocities is not successful.

Checkerboard tests are performed to assess the reliability and lateral resolution of the velocity anomalies obtained from the tomographic inversion. The size (100 km-by-100 km) and amplitudes (±300 m/s) of the checkerboard anomalies represent an average over the obtained anomalies within the entire frequency range. According to Eq. (3), synthetic velocities are calculated for the same virtual source—receiver pairs which are also used in the inversion of measured velocities. As the measured velocities originate from smooth dispersion curves, we cannot simply assume that errors in the data are represented by uncorrelated noise. A more realistic noise model would include a range of smooth variations of the dispersion curves, but that requires an extensive suite of tests which are beyond the scope of this study. Our analysis primarily investigates the robustness of the inversion for the cell velocities with regard to the virtual source–receiver geometry, and the resulting variation of resolution as a function of frequency. We are aware that the absence of noise will provide an over-estimation of the resolution, and thus regard the outcome as an upper limit for our study.

The calculated synthetic velocities are inverted with the same parameters as used in the inversion of measured dispersion curves from vertical and transverse components. The results are shown in Figs. 11 and 12. For the vertical-component geometry (Rayleigh waves; Fig. 11), the area covered by ray paths is mostly recovered in the frequency range up to

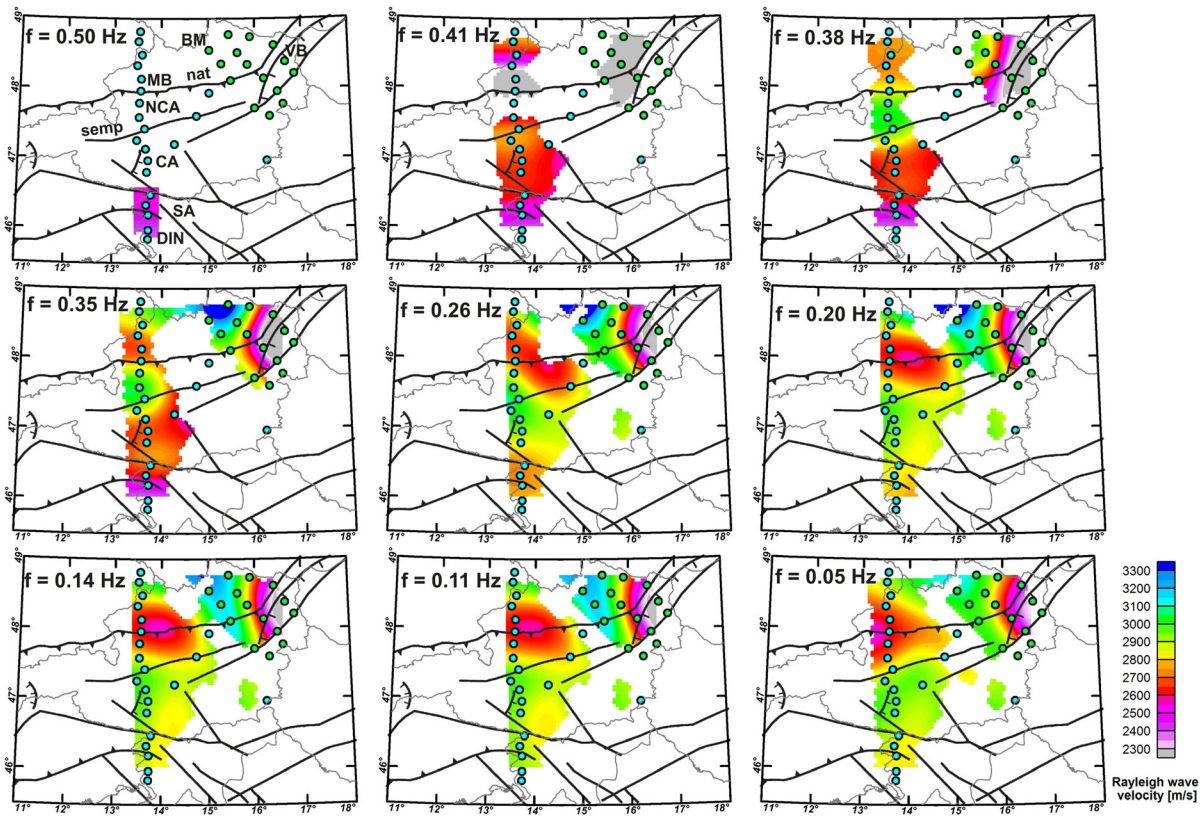

Figure 8
Rayleigh-wave group velocity maps obtained from tomographic inversion of vertical-component dispersion curves. *MB* Molasse basin; *BM* Bohemian Massif; *NCA* Northern Calcareous Alps; *CA* Central Alps; *SA* Southern Alps; *DIN* Dinarides; *VB* Vienna basin; *nat* North Alpine thrust; *semp* Salzach-Enns-Mariazell-Puchberg line. See discussion section for details

0.20 Hz, with the exception of the eastern and northeastern edge. At 0.26 Hz, the resolution also drops in the central part, and at higher frequencies, only the densely sampled area along the profile ALPASS 1 bears some general resemblance with the checkerboard pattern.

The measured dispersion curves from the transverse components (Love waves) were originally inverted with the same damping parameter as used in the inversion for Rayleigh-wave velocities. The resulting velocity maps showed a significantly stronger lateral variation than the Rayleigh-wave velocity maps, and an overall unrealistic velocity distribution. Thus, the damping was increased to stabilize the inversion, leading to the final model (Table 1; Fig. 9) which, however, still is less reliable than the Rayleigh-wave model. The effect of the larger damping parameter is also reflected in the checkerboard test for the transverse-component geometry (Fig. 12), which, in comparison with the vertical-component data (Fig. 11), is also characterized by stronger smearing. An additional checkerboard test with decreased damping was also performed and derived a pattern reconstruction similar to vertical-component geometry. This implies that the coverage and geometry of the input data are not the cause for the implausibility of the inverted Love-wave model. It is more likely that the measured Love-wave dispersion is less-suited for the inversion, since the subsurface structure is too complex to describe Love-wave propagation along straight ray paths. This may be due to the fact that Love waves are more sensitive to the (complex) shallower structure than Rayleigh waves (Dahlen and Tromp 1998), and it is also in accordance with the poor data fit of the inversion (Table 1).

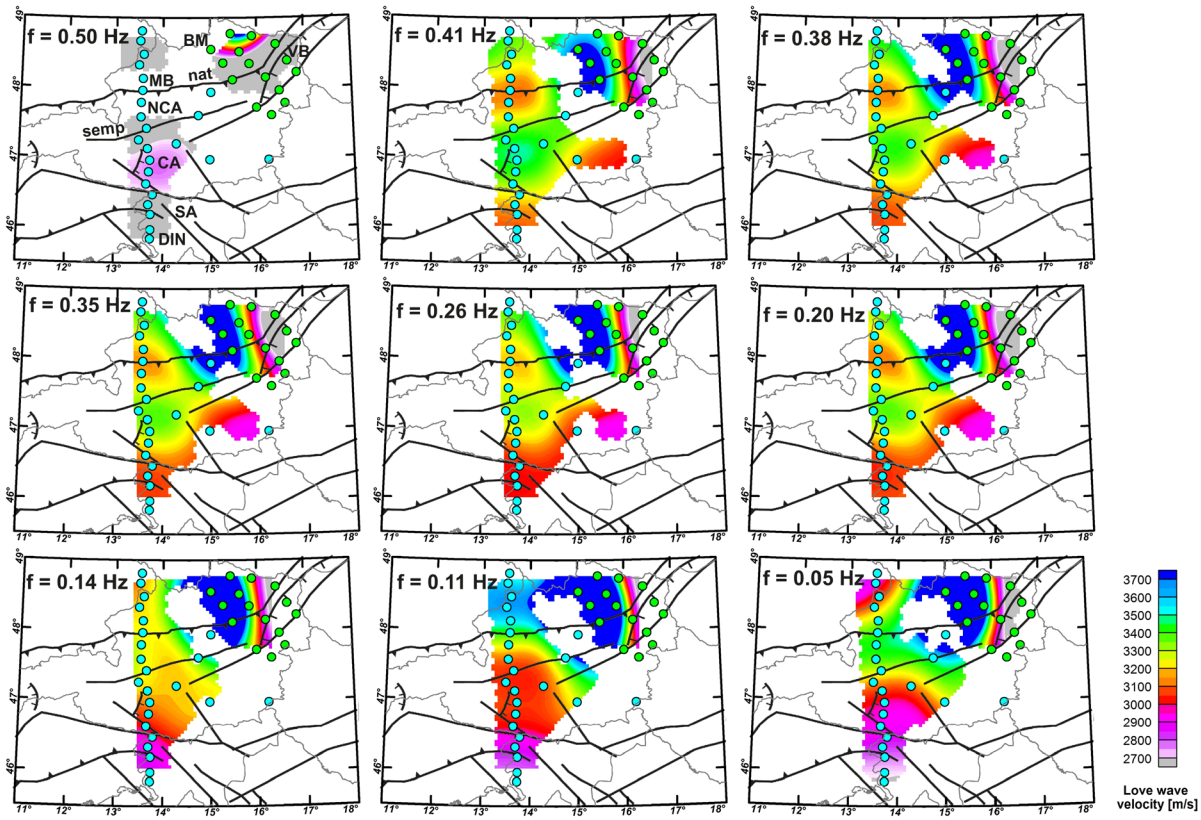

Figure 9
Love-wave group velocity maps obtained from tomographic inversion of transverse-component dispersion curves. Geologic captions as in Fig. 8. See discussion section for details

Table 1

Summary of the results from the inversion for cell velocities, averaged over all inversions in the frequency range 0.05–0.5 Hz

	Min./max./average/std.dev. velocity of input data (measured velocities)	Min./max./average/ std.dev. velocity of the final model	Std.dev. of the starting model misfit	Std.dev. of the final model misfit	Std.dev. reduction (%)
Z-component	1490/4174/2772/282 m/s	1691/3542/2791/278 m/s	238 m/s	168 m/s	30
T-component	1025/5126/2980/519 m/s	1450/6429/3244/465 m/s	642 m/s	537 m/s	16

First column: statistics for input data (=measured dispersion v_{AB}). Second column: Statistics for inversion results (=cell velocities v_{cell}). Third and fourth columns: std.dev. of the residual data misfit (=difference between measured dispersion and modelled dispersion for the initial and final models). Fourth column: reduction of the residual misfit

Finally, virtual dispersion curves are created by fitting a fourth-order polynomial through the obtained cell velocity dispersion curves $v_{cell}(f)$ at each grid point. This is necessary, since velocities obtained at individual frequency nodes can still deviate from a desired smooth dispersion curve due to local variations of inversion quality (Fig. 13). Polynomial fitting is more suitable than smoothing or averaging to remove these outliers, since the curves are preserved where they are smooth and outliers will not distort the

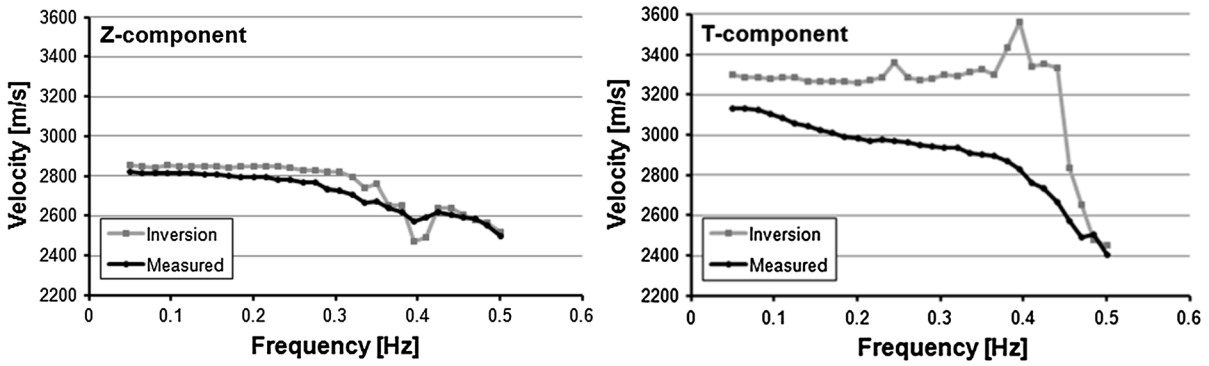

Figure 10
Comparison of average measured surface-wave velocities v_{AB} between stations (*black lines*) and average inverted cell velocities v_{cell} (*grey lines*). The inversion of T-component data (Love waves) is deemed not successful as the average of the velocities after the inversion is significantly different from the average of the measured velocities

virtual dispersion curve significantly. We obtain virtual Rayleigh-wave dispersion curves at 128 locations. Figure 12 indicates that even closely spaced measured dispersion curves may scatter due to laterally variable tectonic structure [e.g., location (3) in the Vienna Basin]. It also illustrates that virtual dispersion can be considered as a physically reasonable 1D approximation to the vertical structure at the cell locations, and that they provide a useful interpolation in areas with pronounced three-dimensional structural variation.

4.3. *Inversion for the Lateral Shear-Wave Velocity Structure Along Profile ALPASS 1*

We calculate the shear-wave velocity structure from the inversion of the virtual dispersion curves of Rayleigh-wave group velocities. Love-wave velocities are not inverted, because their lateral distribution is not well captured by the SIRT-based tomography (Sect. 4.2). Due to the sparse lateral coverage, we apply the inversion for 16 cell locations along the profile ALPASS 1 only. We implement the inversion using the technique in MOKHTAR *et al.* (1988) and HERRMANN (2013). An iterative scheme is used to update the shear-wave velocities to minimize the misfits of virtual and predicted dispersion curves in the frequency range of 0.05–0.5 Hz. The starting model is based on the average P-wave velocity (BEHM *et al.* 2007). This P-wave velocity model was created from stacking and inversion of 3D wide-angle refraction/reflection data acquired within continental active-source seismic refraction campaigns (GUTERCH *et al.* 2003a, b; BRÜCKL *et al.* 2003). It comprises depths to the Moho and a smooth and continuous 3D velocity model of the crust. We extract a vertical section through this model along the profile ALPASS 1. Initial shear-wave velocities are obtained from dividing P-wave velocities by 1.73. Densities are calculated from P-wave velocities by the empirical relationship given by BROCHER (2005). Although we do not set the number of layers for the inversion, we utilize a damping factor to obtain smooth depth variation of velocities. The data fit of the inversion is analysed by comparing the virtual dispersion curves with the predicted dispersion curves from the obtained shear-wave velocities (Fig. 14).

The general trends are well captured, while significant deviations correlate with regions of complicated geology. The profile range $x = 5260$–$x = 5360$ comprises the lateral transition from the Northern Calcareous Alps and Flysch zones to the Molasse basin sediments and crystalline Bohemian Massif, where the shallow vertical structure is characterized by low-angle overthrusting and velocity inversions. The large data misfit at high frequencies is an expression of the intricate seismic structure which cannot be described well with the 1D method. Another general observation is the velocity drop of the modelled dispersion curves at very low

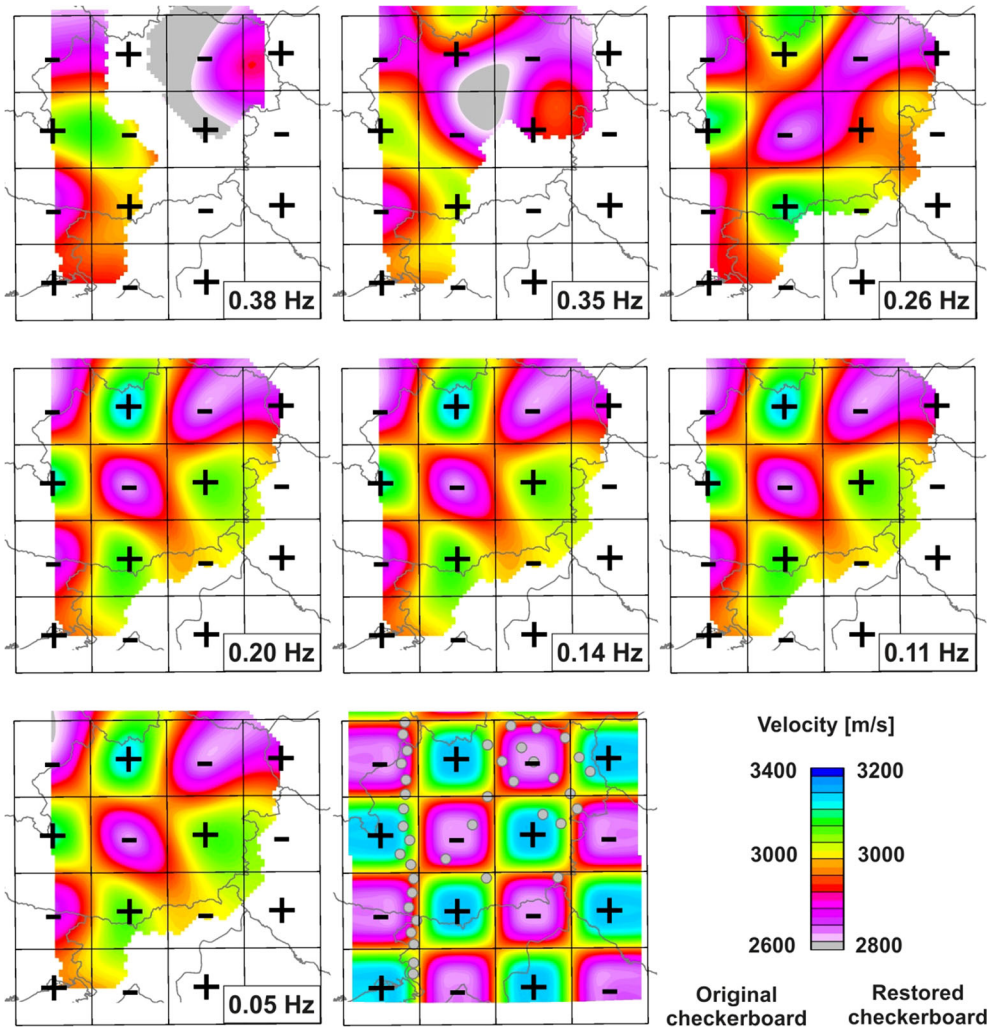

Figure 11
Results from checkerboard tests for vertical-component data. The imposed pattern and the station coverage are shown in the *center* of the *bottom row*. Restored patterns are shown for different frequencies. See text for discussion

frequencies (<0.1 Hz). This might be explained by systematic under-estimation of the measured dispersion due to distortion introduced by non-optimum FTAN parameterization in that frequency range, or due to an overlap of causal and acausal arrivals at short station distances.

Figures 15a-c shows the inverted and interpolated shear-wave velocities together with previously established models from active-source seismology (Behm *et al*. 2007; Behm 2009). Figure 15d is an estimate of the quality of the inversion, as measured by the data misfit between modelled and virtual dispersion:

$$\text{Misfit}(f) = \frac{v_{\text{model}}(f) - v_{\text{virtual}}(f)}{v_{\text{virtual}}(f)} \cdot 100 \qquad (5)$$

At each cell location along the profile, the misfit is plotted at a pseudodepth according to Eq. (6):

$$z(f) = \frac{v_{\text{Avg}}(f)}{f \cdot 3.5} \qquad (6)$$

In Eq. (6), the velocity $v_{\text{Avg}}(f)$ is calculated as the average from all cell velocities for a given frequency f. We further calculate the wavelength for this

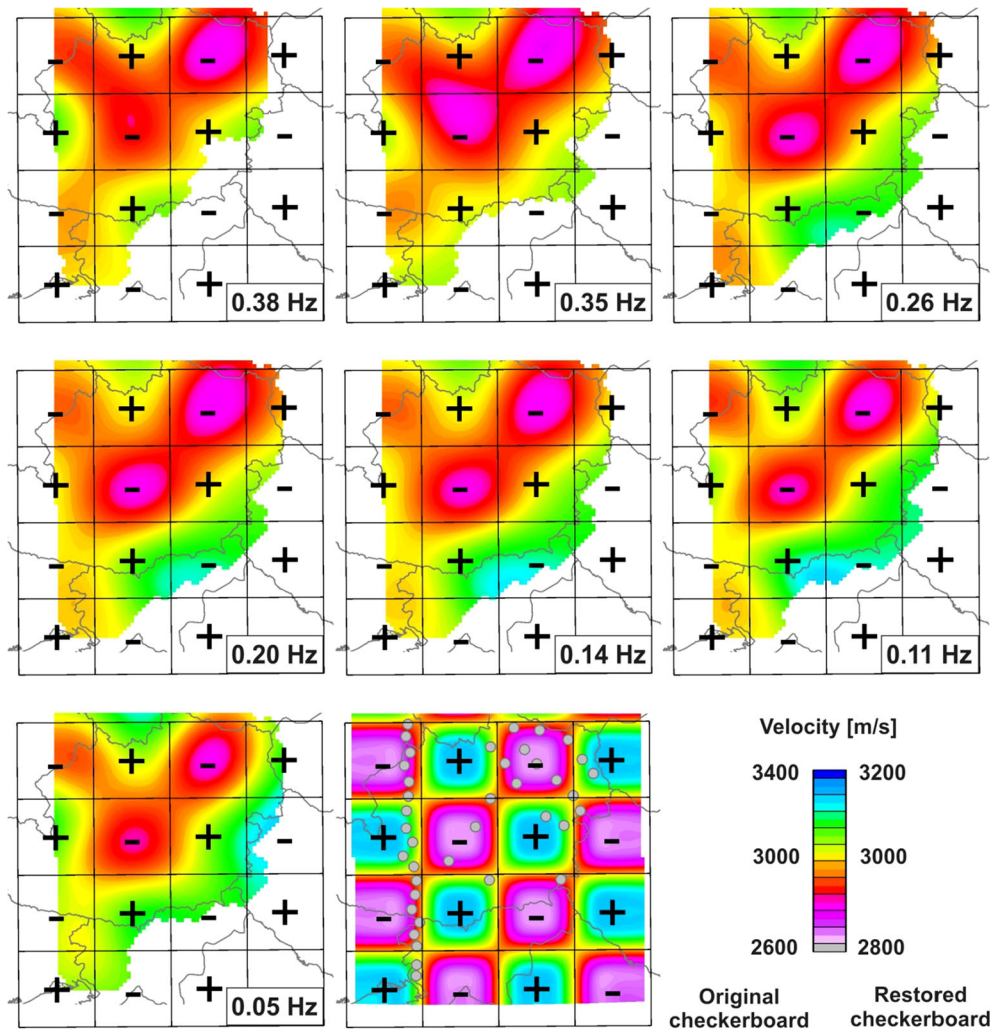

Figure 12
Results from checkerboard tests for transverse-component data. The imposed pattern and the station coverage are shown in the *center* of the *bottom row*. Restored patterns are shown for different frequencies. See text for discussion

velocity and frequency. The sensitivity kernel of surface waves is commonly assumed to peak at depths between a third and a quarter of the wavelength (STEIN and WYSSESION 2003), which makes us chose the factor 3.5 in Eq. (5). With increasing wavelengths, the sensitivity kernel flattens out and the surface-wave velocities are representative of the average crustal velocity between the surface and the depth z. The pseudodepth does not exactly correspond to the depth shown in Fig. 15d, but allows for a rough assessment of the model quality in terms of data fit for shallow vs. deep sections of the crust.

5. Discussion

Prior to the analysis of the shear-wave velocity model, we discuss Rayleigh and Love-wave velocities and their ratio. Rayleigh-wave velocities (Fig. 8) in the frequency range 0.5–0.26 Hz correlate with surface geology. Low velocities are found within the Vienna and Molasse basins, while the NCA and the Greywacke zone in-between the NAT and the SEMP exhibit high velocities. To the very south, the Southern Alps and the Dinarides have lower velocities than the Central Alps to the north. The highest

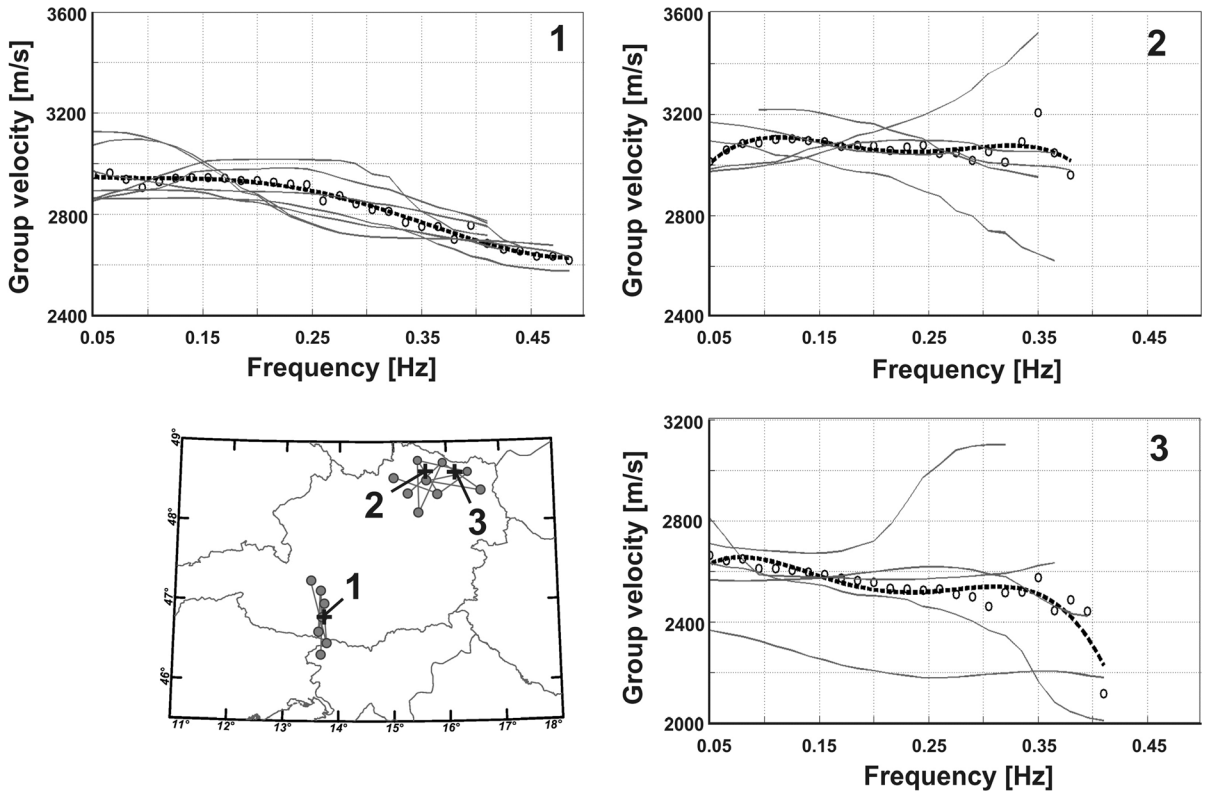

Figure 13
Construction of virtual dispersion curves (*dashed black line*) for given cell locations (*1–3*; *black crosses*) from measured dispersion curves (*solid grey lines*) at nearby virtual source–receiver combinations (*grey dots* and *lines* in the map inlet). *Open black circles* in (*1–3*) are the cell velocities at each frequency bin obtained from tomographic inversion. In the case of strongly scattered input dispersion curves (locations 2 and 3), the virtual dispersion curve resembles a reasonable estimate of the subsurface structure at the cell location. See text for details

velocities are associated with the Bohemian Massif. At lower frequencies (0.2–0.05 Hz), the Alpine crust south of the SEMP appears relatively uniform. The Bohemian Massif and the Vienna Basin exhibit high and low, respectively, velocities throughout the entire frequency range. An extended low-velocity feature is found below the NCA and the Molasse Basin.

The Love-wave maps (Fig. 9) show the same large-scale trend as Rayleigh-wave maps: Low velocities in the Vienna Basin, high velocities in the Bohemian Massif, and a transition from lower to higher velocities when crossing from the Southern Alps to the Central Alps. However, the low-velocity anomaly below the NCA and the Molasse Basin is restricted to higher frequencies. We also find a pronounced high-velocity anomaly throughout all depths associated with the south-eastern tip of the Bohemian Massif, which is not featured in the maps of the

Figure 14 ▶
Virtual (*grey dashed lines*) and predicted (*solid black lines*) Rayleigh-wave dispersion curves from the shear-wave velocity model extracted at 16 locations along the profile ALPASS 1 (Fig. 15). Strong deviations occur at the higher frequencies (*shallow crust*) at the transition from the Eastern Alps to the Bohemian Massif ($x = 5300$–$x = 5400$)

Rayleigh-wave velocities. A spatially coincident high-velocity structure is present in the shear-wave velocity model of Ren *et al*. (2013) which is based on inversion from Rayleigh-wave dispersion. The 3D shear-wave velocity model from active-source data (Behm 2009) also features slightly increased velocities in this region in the shallow crust. High shear-wave velocities would be probably associated with high Love-wave velocities. However, the measured Love-wave velocities in that area are significantly lower than the ones obtained from the SIRT-based

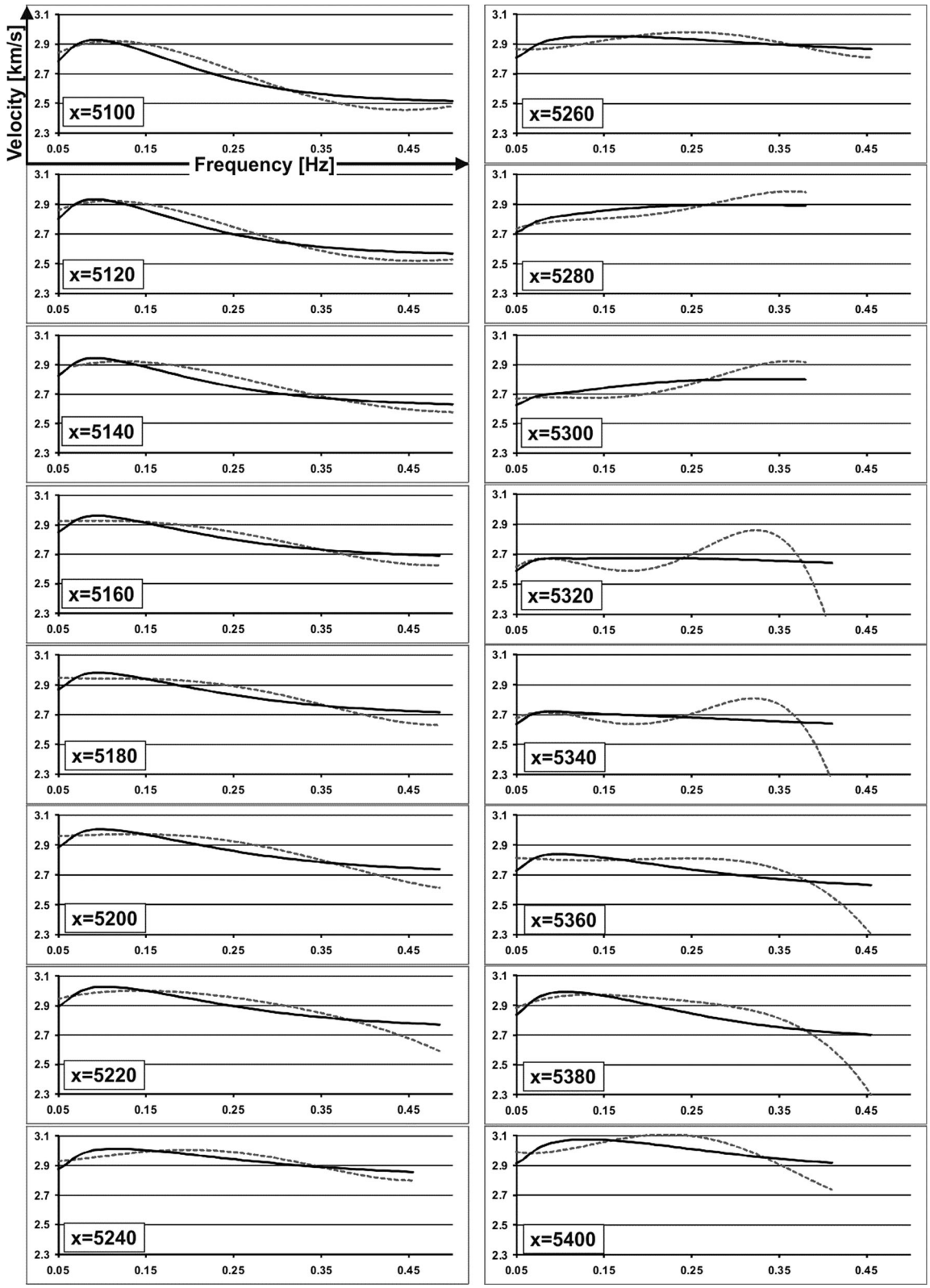
Velocity [km/s]
Frequency [Hz]
x=5100
x=5120
x=5140
x=5160
x=5180
x=5200
x=5220
x=5240
x=5260
x=5280
x=5300
x=5320
x=5340
x=5360
x=5380
x=5400
3.1
2.9
2.7
2.5
2.3
0.05
0.15
0.25
0.35
0.45

tomographic inversion. The latter ones exceed plausible values (>4000 m/s), and the accuracy analysis (Sect. 4.2) indicates a general inferiority of the inversion for Love-wave velocities compared to Rayleigh-wave velocities. The inverted Love-wave velocities are regarded as not reliable in that area. The failure of the inversion for Love-wave velocities based on Eq. (3) could indicate that the modelling of the wave propagation along straight line paths is not appropriate in that area of anomalous crustal structure. The neglect of ray bending in a smooth velocity field would only be relevant for higher frequencies at larger offsets, but strong lateral and vertical velocity contrasts cannot be captured by the intrinsic layer-cake assumption for surface-wave propagation. A thorough analysis would require the modelling of 3D propagation of both Rayleigh and Love waves for different geologic scenarios, which is beyond the scope of our study.

Non-stationary Rayleigh-wave noise sources can contribute to spurious signals on transverse-component interferograms (Kimman and Trampert 2010; Xu *et al*. 2015), which could also account for the failure of the inversion. Tsai (2009), Weaver *et al*. (2009), Froment *et al*. (2010), and Fichtner (2014) analyse the effect of heterogeneous noise distributions on the measured travel times of the surface wave arrivals in Green's functions obtained from ambient noise tomography. They derive the conclusion that the expected travel-time error is relatively small (<1 %) for realistic noise source scenarios and band-limited data sets like ours. However, some dispersion curves in our data set are indicative of more significant systematic deviations from a homogenous noise distribution (Sect. 4.1, Fig. 6d). In this case, the measured surface-wave velocities would be affected and hamper the application of Eq. (3).

Even if the measured group velocities can be correctly described by Eq. (3), they might be picked with large uncertainty in certain areas, e.g. in anomalous crust. The uncertainty is not accounted for in the inversion, since we did not introduce a data covariance matrix (Tarantola 1987), and this might be another reason for the failure of the inversion. Finally, the inversion could be improved by taking the ray coverage into account more systematically. E.g., Bleibinhaus and Gebrande (2006) and Bleibinhaus *et al*. (2010) show how the geometry of the model parameter grid can be iteratively adapted according to their resolution elements.

Average Rayleigh and Love-wave velocities at each frequency are calculated from the measured dispersion curves (Fig. 8), and they show an expected decay with increasing frequency. The average ratio of Love- and Rayleigh-wave velocities in the range of 0.05–0.4 Hz is 1.1. It is noted that the average velocities are calculated for each frequency range over the entire area, thus they as well as their ratio are also biased towards the slightly variable coverage. This applies in particular for the high-frequency end of the dispersion.

In the Vienna Basin, we observe the Rayleigh waves to be faster than Love waves (Sect. 4.1, Fig. 6d). Theoretically, anisotropy can cause Rayleigh waves to be faster than Love waves. However, the region in and around the Vienna Basin is well explored due to local oil and gas exploration (Brix 1993), and by regional seismic transects (e.g. Hrubcová *et al*. 2005; Behm *et al*. 2007; Behm 2009), and significant anisotropy in the upper crust has not been required so far. A recent study by Xu *et al*. (2015) illustrated how non-stationary Rayleigh-wave noise sources can contribute to spurious signals on transverse-component interferograms. Kimman and Trampert (2010) also demonstrate that heterogeneous surface noise source distributions result in significant cross terms in the correlations with the possibility of projecting Love-wave energy on the radial component and vice versa. The metropolitan area of Vienna is a potential source of ambient seismic energy which might emerge as a non-physical signal on interferograms on nearby stations. In addition, the shown virtual source—receiver pair is located at and parallel to the border of low-velocity sediments with high-velocity crystalline rocks, and different components may emphasize different ray paths. Strong lateral material contrasts can also couple Love- and Rayleigh-wave energy (e.g. Maupin and Park 2007).

Finally, we compare and discuss different velocity models along the profile ALPASS 1 (Fig. 15). The shear-wave velocity model from Behm (2009) (Fig. 15a) is obtained from tomographic travel-time inversion from active-source data. The shallow structure correlates with surface geology by imaging

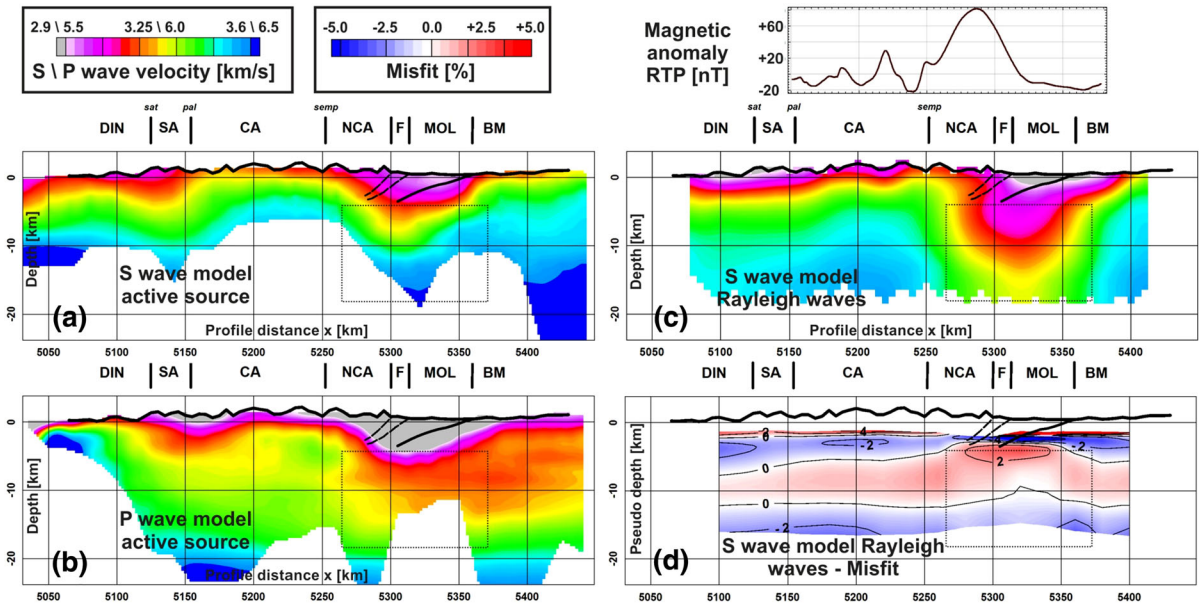

Figure 15

Shear-wave velocity models along the ALPASS 1 profile obtained from different approaches and data sets. *Solid/dashed black lines*: downward extension of the major velocity contrasts NCA/F and MOL/BM based on well and seismic exploration data. *Dashed black rectangle*: low-velocity region discussed in the text. **a** Travel-time tomography from diving S-waves in active-source data (Behm 2009); **b** travel-time tomography from diving P-waves in active-source data (Behm *et al.* 2007); **c** Rayleigh surface-wave dispersion from the ALPASS data set (this study); **d** Misfit analysis of the model (**c**) based on observed vs. predicted dispersion (Fig. 14). The depth axis in (**d**) refers to the pseudodepth and is only a proxy to the actual depth. *Red* and *blue colours* indicate over- and under-estimation, respectively, of observed surface-wave velocities

the low-velocity sediments of the Molasse basin. The Central Alps feature slightly increased velocities. In contrast, the shear-wave model obtained from surface-wave inversion by Ren *et al.* (2013) has its velocity minimum associated with the Central Alps. This appears implausible as this part of the Alps comprises metamorphic rocks with overall larger densities and P-wave velocities than the Neogene sediments in the Molasse basin (Brückl *et al.* 2007; Behm *et al.* 2007; Simeoni and Brückl 2009). It is noted that the model by Ren *et al.* (2013) suffers from low coverage in the Eastern Alps which may explain this discrepancy. Our shear-wave model obtained from Rayleigh waves (Fig. 15c) indicates a gradual thickening of a near-surface low-velocity zone south of the Central Alps, and it positions the low-velocity Molasse sediments correctly. The most interesting feature in this model is a pronounced low-velocity zone below the Molasse basin in depths ranging from 5 to 18 km. Compared with other regions in the model, the misfit (Fig. 15d) is relatively small in this section of the crust. This region also forms the southern rim of the European margin, and relatively moderate-to-low P-wave velocities are also identified in active-source data (Brückl *et al.* 2007; Behm *et al.* 2007). A tentative interpretation of these low velocities as an expression of crustal extension and weakening prior to collision with the Adriatic crust is given by Brückl *et al.* (2007). The absence of this feature in the deeper part of the shear-wave velocity model based on active-source data (Fig. 15a) might be explained by an inversion artefact resulting from low coverage. Due to their high-frequency content, the travel times of shear body waves are more sensitive to small-scale velocity variations, and the under-estimation of shallow high-velocity regions (e.g. Northern Calcareous Alps) might be compensated by over-estimation of deeper structures, in particular when data coverage is low.

The three shear-wave velocity models (Figs. 15a, c; Ren *et al.* (2013), not shown) exhibit both similar and contradicting features at different locations. This

is mainly attributed to the laterally varying coverage of each model. The overall reliability of surface-wave inversion in complex 3D structures is limited, as it is intrinsically based on layered 1D media. To tackle this challenge, dense station coverage is required. Vertical resolution of the surface-wave inversion models is generally low, and the models also depend on assumptions of density and P-wave velocity. On the other hand, first-arrival travel-time tomography tends to smear out lateral velocity contrasts in case of low data coverage. With regard to frequency, the body waves from the active-source data cover a frequency range of roughly 2–10 Hz, while the surface waves comprise a range from ca. 0.1–1 Hz. We suggest that future inversion strategies should aim at joint use of travel-time and surface-wave data to benefit from the complementary resolution and depth penetration capabilities and the broadening of the frequency spectrum.

Figure 16 compares the Rayleigh-wave and P-wave velocity models with the long wavelength part of the magnetic intensity map (Seiberl 1991; Blaumoser 1992). The western part of the magnetic map is dominated by the strong, positive "Berchtesgaden anomaly". Although slightly shifted to the North, the spatial pattern is not unlike that of the Rayleigh-wave velocity model extracted for low frequencies, representing depths larger than 7 km. The low Rayleigh velocities in that area correspond to the shear-wave velocity minimum along the ALPASS 1 profile (Fig. 15c). In addition to the Berchtesgaden anomaly, there is also a visual correlation between the two maps (high magnetic intensity—low seismic velocity) in the East, under

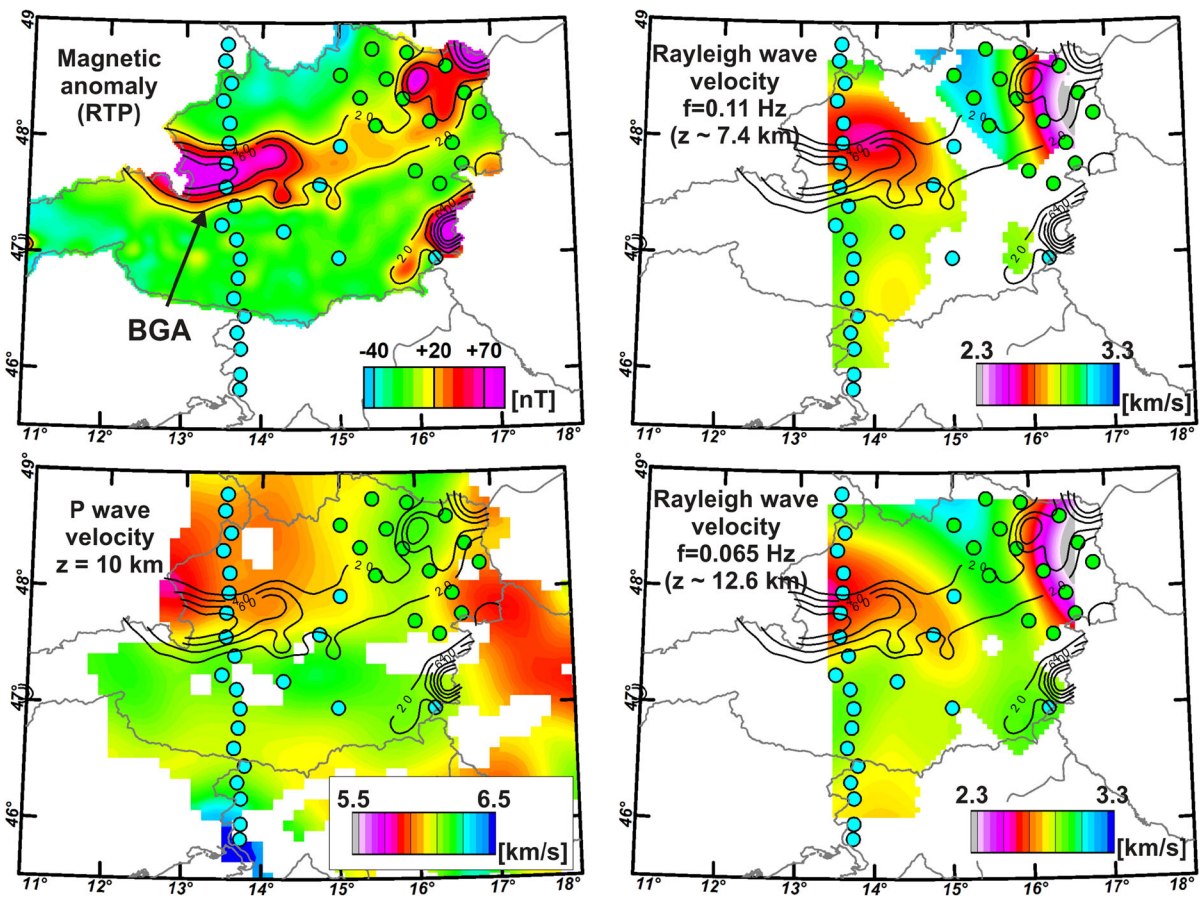

Figure 16
Comparison of magnetic intensity anomaly map (*BGA* = Berchtesgaden anomaly), the 10 km-depth slices through the P-wave velocity model, and pseudodepth slices of the Rayleigh wave velocity model. Isolines of strong magnetic anomalies are superimposed on the velocity slices. See text for discussion

the south-eastern part of the Bohemian massif and west of the Vienna basin region.

The Berchtesgaden anomaly has been studied by Bleil (1976). He suggested two possible interpretations: (1) the anomaly being part of a shallow metamorphic complex of the Bohemian massif, as a part of the Paleo-European plate, and (2) the anomaly representing part of a deeper ancient Tethyan ocean floor. Heinz and Seiberl (1990) and Gnojek and Heinz (1993) also suggest the ophiolithic remnants of oceanic crust as a possible cause for the magnetic anomaly. Reisner (1988) modelled the anomaly along several cross-sections by a southward dipping body of increased susceptibility. Its upper boundary is located between 10 and 16 km-depth, and its thickness is between 2 and 5 km.

If the magnetic and seismic anomalies result indeed from the same source, then one would need to explain though, why high magnetic susceptibility would be correlated with low seismic (shear-wave) velocities. Both of the "classical" interpretations mentioned above (metamorphic basement and oceanic crust) would primarily be associated rather with a positive correlation (e.g., high seismic velocity and magnetic susceptibility). However, there is evidence for the presence of Serpentinites in the Bohemian massif (e.g., Götzinger 1987). Serpentinites are generally associated with low seismic velocities, depending on water content (Christensen 2004; Mookherjee and Stixrude 2013), as well as high magnetic susceptibility (Bina and Henry 1990; Toft *et al*. 1990; Oufi *et al*. 2002). Gravity data are difficult to interpret in the area because of the superposition of several prominent density anomalies (Molasse basin, Flysch, Northern Calcareous Alps, down-dipping European plate). Nonetheless, the low P-wave velocity structure (Fig. 16) at and north to the BGA can also be correlated with a gravity low in the stripped gravity map by Simeoni and Brückl (2009). Therefore, serpentinites might be considered as an explanation for the negative correlation, and would support previous interpretations of the occurrence of oceanic crust at the transition from the Adriatic to the European realm. However, the spatial resolution of our models is not strong enough to strictly require such an explanation at this point.

6. Conclusions

We have applied the ambient noise tomography technique to passive seismic data recorded in the easternmost part of the Alps. Despite a relatively short deployment time, we are able to reconstruct a substantial set of empirical Green's functions comprising Rayleigh and Love waves in the frequency range of 0.1–0.5 Hz. The lateral coverage allows for a tomographic inversion providing virtual dispersion curves which are representative of the vertical seismic structure at a given location. Their combination leads to frequency-dependent maps of Rayleigh and Love-wave velocities which correlate with surface geology. The average ratio of Love- and Rayleigh-wave velocities is 1.1. We find indications that the assumption of homogenous noise source distribution is locally violated in the case of Love waves.

Inversion for shear-wave velocities along a vertical N-S section stretching from the Bohemian Massif through the Central Alps to the Southern Alps, and Dinarides reveals a mid-crustal low-velocity anomaly at the contact between the Bohemian Massif and the Alps. This area is also characterized by large magnetic anomalies and low compressional wave velocity. A possible interpretation is the presence of serpentinite in the upper and middle crust at the transition from the Adriatic to the European realm.

The comparison between velocity models from three different data sets and approaches shows significant differences owing to their varying coverage and complementary resolution capabilities. Certainly, the dense and homogeneous spatial coverage of the (entire Alpine) area in the upcoming AlpArray project (Kissling *et al*. 2014) will be very helpful for resolving these issues. Together with advanced processing and inversion techniques, these data will contribute to an improved understanding of the intricate structure of the Eastern Alps

Acknowledgments

ALPASS was funded by the Austrian Academy of Sciences. We thank the teams and research groups involved in the data collection (Technical University of Vienna, University of Texas at El Paso, University

of Leeds) and the instrument donors (IRIS/UTEP, SEIS-UK, Polish Academy of Sciences, University of Oulu). Yong Ren kindly provided the shear-wave velocity model from the CBP data set. Bruno Meurers (University of Vienna) and Robert Supper (Geological Survey of Austria) helped with obtaining the magnetic anomaly map. We thank Florian Bleibinhaus and one anonymous reviewer for their insightful and constructive comments.

Appendix: list of used stations

	Longitude (°WGS84)	Latitude (°WGS84)	Elevation (m)	Sensor type	Start of recording	Duration (weeks)
CBP						
W1	48.54990	15.01703	749	Guralp 6TD	12.04.2006	71
W2	48.35433	15.27353	671	Guralp 6TD	11.04.2006	71
W3	48.11519	15.47380	316	Guralp 6TD	10.04.2006	71
W5	47.72023	15.97795	555	Guralp 6TD	13.04.2006	71
W6	47.60769	16.29175	755	Guralp 6TD	20.04.2006	70
M1	48.77398	15.43717	567	Guralp 6TD	12.04.2006	71
M2	48.51447	15.62292	389	Guralp 6TD	11.04.2006	72
M3	48.34355	15.83383	197	Guralp 6TD	10.04.2006	72
M4	48.14707	16.17912	358	Guralp 6TD	10.04.2006	72
M5	47.95874	16.46578	208	Guralp 6TD	13.04.2006	72
M6	47.77742	16.58189	187	Guralp 6TD	20.04.2006	71
E1	48.73997	15.89689	309	Guralp 6TD	11.04.2006	72
E2	48.61987	16.40292	296	Guralp 6TD	11.04.2006	73
E3	48.38388	16.64090	189	Guralp 6TD	12.04.2006	73
E4	48.21365	16.82958	152	Guralp 6TD	12.04.2006	73
ALPASS						
D02	48.81345	13.54197	657	Guralp CMG 40T	02.05.2005	47
D03	48.67189	13.51058	469	Guralp CMG 40T	03.05.2005	47
AT104	48.48039	13.58850	532	Guralp CMG 3ESP	03.05.2005	47
AT105	48.32800	13.48961	437	Guralp CMG 40T	04.05.2005	47
AT106	48.13508	13.57431	591	Guralp CMG 40T	04.05.2005	47
AT107	47.96430	13.56648	518	Guralp CMG 40T	05.05.2005	47
AT108	47.79153	13.53883	633	Guralp CMG 40T	04.05.2005	47
AT109	47.58519	13.53537	815	Guralp CMG 40T	04.05.2005	47
AT110	47.42183	13.65145	1176	Guralp CMG 40T	05.05.2005	47
AT111	47.25553	13.48847	1456	Guralp CMG 40T	03.08.2005	34
AT112	47.13319	13.67589	1153	Guralp CMG 40T	04.05.2005	47
AT113	46.96786	13.72625	1676	Guralp CMG 40T	03.05.2005	46
AT114	46.80180	13.70255	862	Guralp CMG 40T	03.05.2005	46
AT115	46.62916	13.64766	1087	Guralp CMG 3ESP	02.05.2005	46
SLO16	46.47453	13.78494	1053	Guralp CMG 40T	04.08.2005	33
SLO17	46.33091	13.69406	963	Guralp CMG 40T	09.05.2005	47
SLO18	46.19150	13.74161	434	Guralp CMG 40T	09.05.2005	47
SLO19	45.97252	13.74130	796	Guralp CMG 40T	10.05.2005	47
SLO20	45.84261	13.73483	360	Guralp CMG 40T	10.05.2005	47
AT202	48.73997	15.89689	280	Guralp CMG 3ESP	23.06.2005	38
AT305	47.93766	15.01161	607	Guralp CMG 3ESP	03.06.2005	42
AT212	47.60695	14.74467	642	Guralp CMG 40T	05.07.2005	36
AT216	47.20367	14.28005	926	Guralp CMG 40T	06.07.2005	36
AT313	46.97170	16.21656	256	Guralp CMG 3ESP	12.05.2005	45
AT601	46.97323	14.98023	1071	Guralp CMG 40T	30.06.2005	38

References

Aki, K. (1957), *Space and time spectra of stationary stochastic waves, with special reference to micro-tremors*, Bulletin of the Earthquake Research Institute *35*, 415–457.

Aki, K., and Richards, P.G. (1980), *Quantitative Seismology*, Vol. I and II, W.H. Freeman, San Francisco.

Bakulin, A., and Calvert, R. (2006), *The virtual source method: Theory and case study*, Geophysics *71*, SI139–SI150.

Behm, M., Brückl, E., Chwatal, W., and Thybo, H. (2007). *Application of stacking and inversion techniques to 3D wide-angle reflection and refraction seismic data of the Eastern Alps*, Geophysical Journal International *170*, 275–298.

Behm, M. (2009), *3-D modelling of the crustal S-wave velocity structure from active source data: application to the Eastern Alps and the Bohemian Massif*, Geophysical Journal International *179*, 265–278.

Behm, M., and Snieder, R. (2013). *Love waves from local traffic noise interferometry*, The Leading Edge *32*, 628–632.

Behm, M., Leahy, G.M., and Snieder, R. (2014), *Retrieval of local surface wave velocities from traffic noise—an example from the La Barge basin (Wyoming)*, Geophysical Prospecting *62*, 223–243.

Bensen, G.D, Ritzwoller, M.H, Barmin, M.P., Levshin, A.L, Lin, F., Moschetti, M.P., Shapiro, N.M., and Yang A. (2007), *Processing seismic ambient noise data to obtain reliable broad-band surface wave dispersion measurements*, Geophysical Journal International, *169*, 1239–1260.

Bianchi, I., and Bokelmann, G. (2014), *Seismic signature of the Alpine indentation, evidence from the Eastern Alps*, Journal of Geodynamics, *82*, 69–77.

Bianchi, I., Miller, M.S., and Bokelmann, G. (2014), *Insights on the upper mantle beneath the Eastern Alps*, Earth and Planetary Science Letters *403*, 199–209.

Bianchi, I., Behm, M., Rumpfhuber, E.M., and Bokelmann, G. (2015), *Moho depths in the Eastern Alps from Receiver Function analysis*, Pure and Applied Geophysics *172*, 2, 295–308.

Bina, M.M., and Henry, B. (1990), *Magnetic properties, opaque mineralogy and magnetic anisotropies of serpentinized peridotites from ODP Hole 670A near the Mid-Atlantic Ridge*, Phys. Earth Planet. Sci. *65*, 88–103.

Blaumoser, N. H. (1992), *Eine erste gesamte aeromagnetische Karte von Österreich und ihre Transformationen*, Mitt. Österr. Geol. Ges./Austrian Journal of Earth Sciences *84*, 185–203.

Bleibinhaus, F., and Gebrande, H. (2006), *Crustal structure in the Eastern Alps along the TRANSALP profile from wide-angle seismic tomography*, Tectonophysics *414*, 51–69.

Bleibinhaus, F., Hilberg, S., and Stiller, M. (2010), *First results from a Seismic Survey in the Upper Salzach Valley, Austria*, Austrian Journal of Earth Sciences *103*/2, 28–32.

Bleil, U., and Pohl, J. (1976), *The Berchtesgaden Magnetic Anomaly*, International Journal of Earth Sciences *65*, 756–767.

Brix, F., 1993, Erdöl und Erdgas in Österreich, Verlag NHM/ F.Berger, Wien/Horn.

Brocher, T. (2005), *Empirical relation between elastic wavespeeds and density in the Earth's crust*, Bulletin of the seismological Society of America *95*, 2081–2092.

Brückl, E., Bodoky, T., Hegedüs E, Hrubcova, P. Gosar, A., Grad, M., Guterch, A., Hajnal, Z., Keller, G.R., Špičák, A., Sumanovac, F., Thybo, H., Weber, F., and ALP 2002 Working Group (2003), *ALP2002 Seismic Experiment*, Studia geophysica geodaetica *47*, 671–679.

Brückl, E., Bleibinhaus, F., Gosar, A., Grad, M., Guterch, A., Hrubcova, P., Keller, G.R., Majdanski, M., Sumanovac, F., Tiira, T., Yliniemi, J., Hegedüs, E., and Thybo, H. (2007), *Crustal structure due to collisional and escape tectonics in the Eastern Alps region based on profiles Alp01 and Alp02 from the ALP 2002 seismic experiment*, Journal of Geophysical Research *112*, B06308.

Brückl, E., Behm,, M., Decker, K., Grad, M., Guterch, A., Keller, G.R., and Thybo, H. (2010), *Crustal structure and active tectonics in the Eastern Alps*, Tectonics *29*, TC2011.

Bussat, S., and Kugler, S. (2009), Feasibility of Offshore Ambient-Noise Surface-Wave Tomography on a Reservoir Scale, 79th International SEG Meeting, Houston, USA, Expanded Abstracts, 1627–1631.

Campillo, M., and Paul A. (2003), *Long-range correlations in the diffuse seismic coda*, Science *299*, 547–549.

Chevrot, S., Sylvander, M., Benahmed, S., Ponsolles, C., Lefevre, J.M., and Paradis D. (2007), *Source locations of secondary microseisms in western Europe: Evidence for both coastal and pelagic sources*. Journal of Geophysical Research *112*, B11301.

Christensen, N.I. (2004), *Serpentinites, peridotites, and seismology*, Int. Geol. Rev. *46*, 795–816.

Dahlen, F.A., Tromp, J., 1998, Theoretical global seismology, Princeton University Press.

Dando, B.D.E., Stuart, G.W., Houseman, G.A., Hegedüs, E., Brückl, E., and Radovanović, S. (2011), *Teleseismic tomography of the mantle in the Carpathian–Pannonian region of central Europe*, Geophysical Journal International *186*, 11–31.

Draganov, D., Campman, X., Thorbecke, J., Verdel, A., and Wapenaar, K. (2009), *Reflection images from ambient seismic noise*, Geophysics *74*, 63–67.

Dziewonski, A.M., Bloch, S., and Landisman, M. (1969). *A technique for the analysis of transient seismic signals*, Bulletin of the seismological Society of America *59*, 427–444.

Cho, K.H., Hermann, R.B., Ammon, C.J., and Lee, K. (2006), *Imaging the crust of the Korean peninsula by surface wave tomography*, Bulletin of the seismological Society of America *97*, 198–207.

Fichtner, A. (2014), *Source and processing effects on noise correlations*, Geophysical Journal International *197*, 1527–1531.

Forghani, F., and Snieder R. (2010), *Underestimation of body waves and feasibility of surface-wave reconstruction by seismic interferometry*, The Leading Edge *29*, 790–794.

Fry, B., Deschamps, F., Kissling, E., Stehly, L., and Giardini, D. (2010), *Layered azimuthal anisotropy of Rayleigh wave phase velocities in the European Alpine lithosphere inferred from ambient noise*, Earth and Planetary Science Letters *297*, 95–102.

Froment, B., Campillo, M., Roux, P., Gouèdard, P., Verdel, A., and Weaver, R.L., (2010), *Estimation of the effect of non-isotropically distributed energy on the apparent arrival time in correlations*, Geophysics *75*, SA85–SA93.

Gardner, L.W. (1939), *An areal plan for mapping subsurface structure by refraction shooting*. Geophysics *4*, 247–259.

Gnojek, I., and Heinz, H. (1993), *Central European (Alpine-Carpathian) belt of magnetic anomalies and its geological interpretation*, Geol. Carpathica *44*, 135–142.

GÖTZINGER, M. (1987), *Mineralogy and genesis of vermiculite in serpentinites of the Bohemian Massif in Austria*, Mineralogy and Petrology *36*, 93–110.

GRAD, M., BRÜCKL, E., MAJDANSKI, M., BEHM, M., GUTERCH, A., and CELEBRATION 2000, ALP 2002, WORKING GROUPS (2009), *Crustal structure of the Eastern Alps and their foreland: seismic model beneath the CEL10/Alp04 profile and tectonic implications*, Geophysical Journal International *177*, 279–295.

GRAßL H., NEUBAUER, F., MILLAHN, K., and WEBER, F. (2004), *Seismic image of the deep crust at the eastern margin of the Alps (Austria): Indications for crustal extension in a convergent origin*, Tectonophysics *380*, 105–122.

GUTDEUTSCH, R., and ARIC, K., Seismicity and neotectonics of the East Alpine-Carpathian and Pannonian Area, In The Pannonian Basin: a study in basin evolution (ed. Royden L.H. and Horvath F.) (AAPG Memoir 45, American Association of Petroleum Geologists and Hungarian Geological Society, Tulsa, Oklahoma, Budapest 1988) pp. 183–194.

GUTERCH, A., GRAD, M., ŠPIČÁK, A., BRÜCKL, E., HEGEDÜS, E., KELLER, G.R., THYBO, H., and CELEBRATION 2000, ALP 2002, SUDETES 2003 Working Groups, (2003a), *An overview of recent seismic refraction experiments in Central Europe*, Stud. Geophys. Geod. *47*, 651– 657.

GUTERCH, A., GRAD, M.,KELLER, G.R., POSGAY, K.,VOZAR, J., ŠPIČÁK, A., BRÜCKL, E., HAJNAL, Z., THYBO, H., SELVI, O., and CELEBRATION 2000 EXPERIMENT TEAM, (2003b), CELEBRATION 2000 Seismic Experiment, Stud. Geophys. Geod. *47*, 659–669.

HALLIDAY, D., and CURTIS, A. (2008), *Seismic interferometry, surface waves and source distribution*, Geophysical Journal International *175*, 1067–1087.

HARMON, N., RYCHERT., C., and GERSTOFT, P. (2010), *Distribution of noise sources for seismic interferometry*, Geophysical Journal International *183*, 1470–1484.

HEINZ, H., and SEIBERL, W. (1990), *Magnetic structures of the eastern Alps west of the Tauern window*, Mém. Soc. géol. France *156*, 123–128.

HERRMANN, R. B. (2013), *Computer programs in seismology: An evolving tool for instruction and research*, Seismological Research Letters *84*, 1081–1088.

HINSCH, R., and DECKER, K. (2003), *Do seismic slip deficits indicate an underestimated earthquake potential along the Vienna Basin Transfer Fault System?*, Terra Nova *15*, 343–349.

HRUBCOVÁ, P., ŚRODA, P., ŠPIČÁK, A., GUTERCH, A., GRAD, M., KELLER, G. R., BRÜCKL, E., and THYBO, H. (2005), *Crustal and uppermost mantle structure of the Bohemian Massif based on CELEBRATION 2000 data*, Journal of Geophysical Research *110*, B11305.

IWASAKI T. (2002), *Extended time-term method for identifying lateral structural variations from seismic refraction data*, Earth Planets Space *54*, 663–677.

KEDAR, S., LONGUET-HIGGINS, M., WEBB F., GRAHAM, N., CLAYTON, R., and JONES, C. (2008), *The origin of deep ocean microseisms in the North Atlantic Ocean*, Proc. R. Soc. London, Ser. A. *464*, 777–793.

KIMMAN, W. P., TRAMPERT, J. (2010), *Approximations in seismic interferometry and their effects on surface waves*, Geophysical Journal International *182*, 461–476.

KISSLING, E., HETENYI., G., and ALPARRAY WORKING GROUP (2014), *AlpArray – Probing Alpine geodynamics with the next generation of geophysical experiments and techniques*, Geophysical Research Abstracts *16*, EGU2014–7065.

FRIEDRICH, A., KRÜGER, F., and KLINGE, K. (1998), *Ocean-generated microseismic noise located with the Grafenberg array*, Journal of Seismology *47*, 47–64.

LANDES, M., HUBANS, F., SHAPIRO, N.M., PAUL, A., and CAMPILLO, M. (2010), *Origin of deep ocean microseisms by using teleseismic body waves*, Journal of Geophysical Research *115*, B05302.

LEVSHIN, A.L., YANOVSKAYA, T.B., LANDER, A.V., BUKCHIN, B.G., BARMIN, M.P., RATNIKOVA, L.I., and IITS, E.N. (1989), *Seismic Surface Waves in a Laterally Inhomogeneous Earth*, Modern Approaches in Geophysiscs, ED. KEILIS-BOROK V.I. KLUWER. ISBN 0-7923-0044-0.

LI, H., BERNARDI, F., and MICHELINI, A. (2010a), *Surface wave dispersion measurements from ambient seismic noise analysis in Italy*, Geophysical Journal International *180*, 1242–1252.

LI, H., BERNARDI, F., and MICHELINI, A. (2010b), *Love wave tomography in Italy from seismic ambient noise*, Earthquake Science *23*, 487–495.

LIN, F.-C., RITZWOLLER, M.H., TOWNEND, J., SAVAGE, M., and BANNISTER, S. (2007), *Ambient noise Rayleigh wave tomography of New Zealand*, Geophysical Journal International *170*, 649–666.

LIN F., MOSCHETTI M.P., and RITZWOLLER M.H. (2008), *Surface wave tomography of the western United States from ambient seismic noise: Rayleigh and Love wave phase velocity maps*, Geophysical Journal International *169*, 1239–1260.

LIPPITSCH, R., KISSLING, E., and ANSORGE, J. (2003), *Upper mantle structure beneath the Alpine orogen from high-resolution teleseismic tomography*, Journal of Geophysical Research *108*, B2376.

LOBKIS, O., and WEAVER, R. (2001), *On the emergence of the Green's function in the correlations of a diffuse field*, The Journal of the Acoustical Society of America *110*, 3011–3017.

LONGUET-HIGGINS, M. S. (1950), *A theory of the origin of microseisms*, Philos.Trans. R. Soc. London, Ser. A *243*, 1–35.

LÜSCHEN, E., BORRINI, D., GEBRANDE, H., LAMMERER, B., MILLAHN, K., NEUBAUER, F., NICOLICH, R., and TRANSALP WORKING GROUP (2006), *TRANSALP - deep crustal Vibroseis and explosive seismic profiling in the Eastern Alps*, Tectonophysics *414*, 9–38.

MACQUET, M., PAUL, A., PEDERSEN, H.A., VILLASENOR, A., CHEVROT, S., SYLVANDER, M., WOLYNIEC D., AND PYROPE WORKING GROUP (2014), *Ambient noise tomography of the Pyrenees and the surrounding regions: inversion for a 3-D Vs model in the presence of a very heterogeneous crust*, Geophysical Journal International *199*, 402–415.

MAUPIN, V., PARK, J. (2007), Chapter 1.09 Theory and Observations—Wave Propagation in Anisotropic Media. In Treatise on Geophysics, G. Schubert, (ed.), Elsevier, Amsterdam, 2007, 289–321.

MITTERBAUER, U., BEHM, M., BRÜCKL, E., LIPPITSCH, R., GUTERCH, A., KELLER, G.R., KOSLOVSKAYA, E., RUMPFHUBER, E-M., and ŠUMANOVAC, F. (2011), *Shape and origin of the East-Alpine slab constrained by the ALPASS teleseismic model*, Tectonophysics *510*, 195–206.

MOKHTAR, T. A., HERRMANN, R. B., and RUSSEL, D. R. (1988), *Seismic velocity and Q model for the shallow structure of the Arabian shield from short-period Rayleigh waves*, Geophysics *53*, 1379–1387.

MOOKHERJEE, M., and STIXRUDE, L. (2013), *Structure and elasticity of serpentine at high-pressure*, Earth Planet. Sc. Lett. *279*, 11–19.

MOSCHETTI, M.P., RITZWOLLER, M.H. and SHAPIRO, N.M. (2007), *Surface wave tomography of the western United States from*

ambient seismic noise: Rayleigh wave group velocity maps, Geochem. Geophys. Geosyst. *8*, Q08010.

Nakata, N., Snieder, R., and Behm M., (2014), *Body-wave interferometry using regional earthquakes with multidimensional deconvolution after wavefield decomposition at free surface*, Geophys. J. Int., *199*, 1125–1137.

Nakata, N., Snieder, R., Tsuji, T., Larner, K., and Matsuoka, T., (2011), *Shear-wave imaging from traffic noise using seismic interferometry by cross-coherence*, Geophysics *76*, SA97–SA106.

Nakata, N., Chang, J. P., Lawrence, J. F., and Boue, P. (2015), *Body-wave extraction and tomography at Long Beach, California, with ambient-noise tomography*, Journal of Geophysical Research *120*, 1159–1173.

Olivier, G., Brenguier, F., Campillo, M., Lynch, R., and Roux, P. (2015), *Body-wave reconstruction from ambient seismic noise correlation in an underground mine*, Geophysics *80*(3), KS11–KS25.

Oufi, O., Cannat, M., and Horen, H. (2002), *Magnetic properties of variably serpentinized abyssal peridotites*, Journal of Geophysical Research *107*, 19.

Peresson, H., and Decker, K. (1997), *Far-field effect of late Miocene subduction in the Eastern Carpathians: E - W compression and inversion of structures in the Alpine–Carpathian–Pannonian region*, Tectonics *16*, 38–56.

Picozzi M., Parolai S., Bindi D., and Strollo A. (2009), *Characterization of shallow geology by high-frequency seismic noise tomography*, Geophysical Journal International *176*, 164–174.

Prieto, G., Lawrence, J.F, and Beroza, G.C. (2009), *Anelastic Earth Structure from the Coherency of the Ambient Seismic Field*, Journal of Geophysical Research *114*, B07303.

Qorbani, E., Kurz, W., Bianchi, I., Bokelmann, G. (2015), *Correlated crustal and mantle deformation in the Tauern Window, Eastern Alps*, Austrian Journal of Earth Sciences, *108*/1, 161–173.

Ratschbacher, L., Frisch, W., Linzer, H. G., and Merle, O. (1991), *Lateral extrusion in the Eastern Alps. 2: Structural analysis*, Tectonics *10*, 257–271.

Rawlinson, N. and Sambridge, M. (2003), *Seismic traveltime tomography of the crust and lithosphere*, Advances in Geophysics *46*, 81–198.

Reisner, M. (1988), Ein Beitrag zur Komplexinterpretation für den Kohlenwasserstoffaufschluss in den Nördlichen Kalkalpen, Master thesis, Montanuniversität Leoben.

Ren, Y., Grecu, B., Stuart, G., Houseman, G., Hegedüs, E., and South Carpathian Project Working Group (2013), *Crustal structure of the Carpathian–Pannonian region from ambient noise tomography*, Geophysical Journal International *195*, 1351–1369.

de Ridder, S., and Dellinger J. (2011), *Ambient seismic noise eikonal tomography for near-surface imaging at Valhall*, The Leading Edge *30*, 1–7.

Roux, P., Sabra, K.G., Kuperman, W.A., and Roux, A. (2005), *Ambient noise crosscorrelation in free space: theoretical approach*, Journal of the Acoustical Society of America *117*(1), 79–84.

Royden, L.H. (1993), *Evolution of retreating subduction boundaries formed during continental collision*, Tectonics *12*, 629–638.

Ruzek, B., Plomerova, J., and Babuska, V. (2012), *Joint inversion of teleseismic P waveforms and surface-wave group velocities from ambient seismic noise in the Bohemian Massif*, Stud. Geophys. Geod. *56*, 107–140.

Schimmel, M., Stutzmann, E., and Gallart, J. (2011a), *Using instantaneous phase coherence for signal extraction from ambient noise data at a local to a global scale*, Geophysical Journal International *184*, 494–506.

Schimmel, M., Stutzmann, E., Ardhuin, F., and Gallart, J. (2011b), *Polarized Earth's ambient microseismic noise*, Geochem. Geophys. Geosyst. *12*, Q07014.

Schmid, S., Fügenschuh, B., Kissling, E., and Schuster, R. (2004), *Tectonic map and overall architecture of the Alpine orogen*. Swiss J. Geosci., *97*, 93–117.

Schuster, G. T. (2010), Seismic Interferometry, Cambridge University Press, Cambridge.

Seiberl, W. (1991), Aeromagnetische Karte der Republik Österreich 1:1,000.000 (Isanomalen der Totalintensität), Geological Survey of Austria.

Shapiro, N.M, Campillo, M., Stehly, L., and Ritzwoller, M.H. (2005), *High resolution surface wave tomography from ambient seismic noise*, Science *307*, 1615–1618.

Simeoni, O., and Brückl, E., 2009, *The effect of gravity stripping on the resolution of deep crustal structures in the Eastern Alps and surroundings Regions*, Austrian Journal of Earth Sciences *102*, 157–169.

van der Sluis, A., and van der Horst, H.A. 1987, Numerical solution of large, sparse linear algebraic systems arising from tomographic problems, In: Seismic Tomography (ed. Nolet G., and Reidel D.) (Hingham, 1987) pp. 49–83.

Snieder, R. (2004), *Extracting the Green's function from the correlation of coda waves: a derivation based on stationary phase*, Phys. Rev. E *69*, 046610.

Snieder, R. (2007), *Extracting the Green's function of attenuating heterogeneous acoustic media from uncorrelated waves*, Journal of the Acoustical Society of America *121*, 2637–2643.

Stehly, L., Campillo, M., and Shapiro, N.M. (2006), *A study of seismic noise from its long range correlation properties*, Journal of Geophysical Research *111*, B10206.

Stehly L., Fry, B.,M. Campillo, M., Shapiro, N.M., Guilbert, J., Boschi, L., and Giardini, D. (2009), *Tomography of the Alpine region from observations of seismic ambient noise*, Geophysical Journal International *178*, 338–350.

Stein, S., and Wyssesion, M. (2003), *An introduction to seismology, earthquakes, and earth structure*. Blackwell publishing.

Tarantola, A. (1987), *Inverse Problem Theory*, Elsevier Scientific Publishing Company, New York.

Telford, W.M., Geldart, L.P., and Sheriff, R.E. (1990), *Applied Geophysics*, 2nd edn., Cambridge University Press, Cambridge.

Toft, P.B., Arkani-Hamed, J., and Haggerty, S.E. (1990), *The effects of serpentinization on density and magnetic susceptibility: a petrophysical model*, Phys. Earth Planet. Inter. *65*, 137–157.

Tsai, V.C. (2009), *On establishing the accuracy of noise tomography traveltime measurements in a realistic medium*, Geophysical Journal International *178*, 1555–1564.

Tsai, V. (2011), *Understanding the amplitudes of noise correlation measurements*, Journal of Geophysical Research *116*, B09311.

Verbeke, J., Boschi, L., Stehly, L., Kissling, E., and Michelini, A. (2012), *High-resolution Rayleigh-wave velocity maps of central Europe from a dense ambient-noise data set*, Geophysical Journal International *188*, 1173–1187.

Villasenor, A., Yang, Y., Ritzwoller, M.H., and Gallart, J. (2007), *Ambient noise surface wave tomography of the Iberian*

Peninsula: Implications for shallow seismic structure, Geophysical Research Letters *34*, L11304.

WAPENAAR, K. (2004), *Retrieving the elastodynamic Green's function of an arbitrary inhomogeneous medium by cross correlation*, Phys. Rev. Lett. *93*, 254301.

WAPENAAR, K., DRAGANOV, D., SNIEDER, R., CAMPMAN, X, and VERDEL, A. (2010a), *Tutorial on seismic interferometry: Part 1 – Basic principles and applications*, Geophysics *75*, 75A195–75A209.

WAPENAAR K., SLOB E., SNIEDER, R., and CURTIS, A. (2010b), *Tutorial on seismic interferometry: Part 2 – Underlying theory and advances*, Geophysics *75*, 75A211–75A227.

WEAVER, R., FROMENT, B., CAMPILLO, M. (2009), *On the correlation of non-isotropically distributed ballistic scalar diffuse waves*, The Journal of the Acoustical Society of America, *126*, 1817–1826.

XU, Z., XIA, J., LUO, Y., CHENG, F., and PAN, Y. (2015), *Potential Misidentification of Love-Wave Phase Velocity Based on Three-Component Ambient Seismic Noise*, Pure and Applied Geophysics, available online.

YANG, Y., RITZWOLLER, M.H., LEVSHIN, A.L., and SHAPIRO, N.M. (2007), *Ambient noise Rayleigh wave tomography across Europe*, Geophysical Journal International *168*, 259–274.

YANG, Y., RITZWOLLER, M.H., LIN., F.-C., MOSCHETTI, M.P., and SHAPIRO, N.M. (2008), *Structure of the crust and uppermost mantle beneath the western United States revealed by ambient noise and earthquake tomography*, Journal of Geophysical Research *113*, B12310.

YANG, Y., and M. H. RITZWOLLER (2008), *Teleseismic surface wave tomography in the western U.S. using the Transportable Array component of USArray*, Geophysical Research Letters *35*, L04308.

YAO, H., VAN DER HILST, R.D., and DE HOOP, M.V. (2006), *Surface-wave tomography in SE Tibet from ambient seismic noise and two-station analysis: I.—Phase velocity maps*, Geophysical Journal International *166*, 732–744.

(Received September 26, 2015, revised April 25, 2016, accepted May 4, 2016)